

*Herschel**-ATLAS: correlations between dust and gas in local submm-selected galaxies

N. Bourne,^{1†} L. Dunne,² G. J. Bendo,³ M. W. L. Smith,⁴ C. J. R. Clark,⁴
D. J. B. Smith,⁵ E. E. Rigby,⁶ M. Baes,⁷ L. L. Leeuw,⁸ S. J. Maddox,²
M. A. Thompson,⁵ M. N. Bremer,⁹ A. Cooray,¹⁰ A. Dariush,¹¹ G. de Zotti,^{12,13}
S. Dye,¹ S. Eales,⁴ R. Hopwood,^{14,15} E. Ibar,¹⁶ R. J. Ivison,¹⁷ M. J. Jarvis,^{18,19}
M. J. Michałowski,^{7,20} K. Rowlands,¹ E. Valiante⁴

¹*School of Physics & Astronomy, University of Nottingham, University Park, Nottingham NG7 2RD, UK*

²*Department of Physics & Astronomy, University of Canterbury, Christchurch, New Zealand*

³*Jodrell Bank Centre for Astrophysics, University of Manchester, Alan Turing Building, Manchester M13 9PL, UK*

⁴*School of Physics & Astronomy, Cardiff University, Queen's Buildings, The Parade, Cardiff CF24 3AA, UK*

⁵*Centre for Astrophysics Research, STRI, University of Hertfordshire, College Lane, Hatfield AL10 9AB, UK*

⁶*Leiden Observatory, J.H. Oort Building, P.O. Box 9513, NL-2300 RA Leiden, The Netherlands*

⁷*Sterrenkundig Observatorium, Universiteit Gent, Krijgslaan 281 S9, B-9000 Gent, Belgium*

⁸*College of Graduate Studies, University of South Africa, P. O. Box 392, Unisa, 003, South Africa*

⁹*H. H. Wills Physics Laboratory, University of Bristol, Tyndall Avenue, Bristol BS8 1TL, UK*

¹⁰*Department of Physics and Astronomy, University of California, Irvine, CA 92697, USA*

¹¹*Institute of Astronomy, University of Cambridge, Madingley Road, Cambridge CB3 0HA, UK*

¹²*INAF-Osservatorio Astronomico di Padova, Vicolo Osservatorio 5, I-35122 Padova, Italy*

¹³*SISSA, Via Bonomea 265, I-34136 Trieste, Italy*

¹⁴*Physics Department, Imperial College London, South Kensington Campus, London SW7 2AZ, UK*

¹⁵*Department of Physical Sciences, The Open University, Milton Keynes MK7 6AA, UK*

¹⁶*Instituto de Astrofísica, Facultad de Física, Pontificia Universidad Católica de Chile, Casilla 306, Santiago 22, Chile*

¹⁷*UK Astronomy Technology Centre, The Royal Observatory, Blackford Hill, Edinburgh EH9 3HJ, UK*

¹⁸*Astrophysics, Department of Physics, Keble Road, Oxford OX1 3RH, UK*

¹⁹*Department of Physics, University of the Western Cape, Private Bag X17, Bellville 7535, South Africa*

²⁰*SUPA, Institute for Astronomy, University of Edinburgh, Royal Observatory, Edinburgh, EH9 3HJ, UK*

22 August 2013

ABSTRACT

We present an analysis of CO molecular gas tracers in a sample of 500 μm -selected *Herschel*-ATLAS galaxies at $z < 0.05$ ($cz < 14990 \text{ km s}^{-1}$). Using 22–500 μm photometry from *WISE*, *IRAS* and *Herschel*, with HI data from the literature, we investigate correlations between warm and cold dust, and tracers of the gas in different phases. The correlation between global CO(3–2) line fluxes and FIR–submm fluxes weakens with increasing IR wavelength ($\lambda \gtrsim 60 \mu\text{m}$), as a result of colder dust being less strongly associated with dense gas. Conversely, CO(2–1) and HI line fluxes both appear to be better correlated with longer wavelengths, suggesting that cold dust is more strongly associated with diffuse atomic and molecular gas phases, consistent with it being at least partially heated by radiation from old stellar populations. The increased scatter at long wavelengths implies that sub-millimetre fluxes are a poorer tracer of SFR. Fluxes at 22 and 60 μm are also better correlated with diffuse gas tracers than dense CO(3–2), probably due to very-small-grain emission in the diffuse interstellar medium, which is not correlated with SFR. The FIR/CO luminosity ratio and the dust mass/CO luminosity ratio both decrease with increasing luminosity, as a result of either correlations between mass and metallicity (changing CO/H₂) or between CO luminosity and excitation [changing CO(3–2)/CO(1–0)].

Key words: galaxies: ISM – infrared: galaxies – radio lines: galaxies – submillimetre: galaxies

1 INTRODUCTION

The cold interstellar medium (ISM) is a vital building block of galaxies, and building up an observational understanding of its properties and processes presents one of the current challenges for astronomy. Dense molecular gas, which fuels star formation, has traditionally been observed in galaxies using the emission lines of the CO molecule, but this tracer is fraught with uncertainties due to varying metallicity and optical thickness (e.g. Dickman, Snell & Schloerb 1986; Genzel et al., 2012). These problems can only be surmounted by the calibration of the CO tracer against independent molecular gas tracers, such as the ISM cooling lines of carbon (Malhotra et al., 2001; Pierini et al. 2001). A more widely available tracer is the dust mass, which is correlated with the H₂ mass assuming a dust-to-gas ratio that is dependent on metallicity (e.g. Cox, Kruegel & Mezger 1986; Issa, MacLaren & Wolfendale 1990; Dunne et al. 2000; James et al. 2002). However, the relationship between metallicity and dust-to-gas ratio is a matter of active research in studies of local spiral galaxies (Draine et al., 2007; Muñoz-Mateos et al., 2009; Bendo et al., 2010b; Magrini et al., 2011; Leroy et al., 2011, 2013; Smith et al., 2012b) and dwarfs (Lisenfeld & Ferrara 1998; Walter et al., 2007).

The revolution in wide-field imaging at far-infrared (FIR) to sub-millimetre (submm) wavelengths, provided by telescopes such as *Herschel* (Pilbratt et al., 2010), means that we now have unprecedented coverage of the spectral energy distribution (SED) of dust in galaxies at both low and high redshifts. We must learn how to interpret these observations in terms of the ISM mass and star-formation activity within galaxies. Emission from dust in star-forming galaxies (SFGs) is dominated by large grains in thermal equilibrium, comprising a number of different phases including a cold (~ 20 K), diffuse component and a warmer (~ 50 K) component associated with star-forming regions (de Jong et al. 1984; Dunne & Eales 2001). Emission from these warm dust grains is directly correlated with the star-formation rate (SFR) since it is heated by emission from young, massive stars (Kennicutt 1998b; Kennicutt & Evans 2012). It is less clear whether the emission from cold dust is directly tied to the SFR, since it is likely to be partially heated by emission from the older stellar population (e.g. Helou 1986; Walterbos & Greenawalt 1996; Bendo et al., 2010a, 2012; Boquien et al., 2011; Totani et al. 2011; Groves et al., 2012; Smith et al. 2012b).

The Schmidt-Kennicutt law (SK law; Schmidt 1959; Kennicutt 1998a) describes a universal correlation in the surface densities of gas (usually H₂) and SFR in galactic disks, with a non-linear slope and a significant amount of scatter. The slope depends on the emission line used to trace the gas, since higher-energy transitions occur in denser and hotter gas (Gao & Solomon 2004; Krumholz & Thompson 2007; Narayanan et al. 2008), and it is this dense gas that directly feeds star formation. Observations show that starbursts and high-redshift submm galaxies (SMGs) deviate

from the SK law of disk galaxies, either as a result of sampling bias favouring the upper end of the intrinsic scatter, or due to a difference in the CO-to-H₂ conversion factor in extreme environments (Daddi et al., 2010; Genzel et al., 2010; Narayanan et al. 2012; Krumholz, Dekel & McKee 2012; Feldmann, Gnedin & Kravtsov 2012). It has been suggested, however, that this observation results from of an excitation bias in using lines with differing excitation energies (Ivison et al. 2011). It also depends upon the assumption that IR luminosities trace the SFR consistently at high and low luminosities, but an increased contribution from dust heated by older stars could affect the apparent SFRs of lower-luminosity galaxies in relation to high-luminosity starbursts and SMGs.

It is important to understand the gas-SFR relationship in SFGs of all luminosities, and to explore the biases resulting from different selection functions. In this paper we compare measurements at FIR wavelengths ($\lambda < 200 \mu\text{m}$), which are sensitive to warmer dust, and submm wavelengths ($\lambda > 200 \mu\text{m}$), which trace the more massive cold dust component (Dunne & Eales 2001). Far-infrared selection favours high-SFR galaxies but does not necessarily select galaxies with massive ISM content. This is likely to be biased towards galaxies in the upper extreme of the SK scatter, characterised by starbursts with high star-formation efficiencies and short gas depletion times. We instead sample nearby galaxies with high dust masses by selecting in the submm, which is an unbiased tracer of the cold ISM. Continuum emission in the submm is a strong tracer of the dust mass and is connected to the total gas mass via the dust/gas ratio, and to the SFR via the SK law. A blind submm survey is therefore much less sensitive to the star-formation properties of galaxies than samples selected at shorter FIR wavelengths (e.g. Yao et al. 2003; Gao & Solomon 2004), and provides a more direct selection of gas-rich galaxies than targeted surveys based on characteristics such as visual morphology (e.g. Young et al., 1995; Helfer et al. 2003; Mao et al. 2010).

Little is known about galaxies selected in this way since before *Herschel* it was impossible to conduct blind sky surveys at $\lambda > 100 \mu\text{m}$ that sample a sufficiently large volume at low redshift. The largest local submm survey prior to *Herschel* was the SCUBA Local Universe Galaxy Survey (SLUGS), which used the SCUBA camera to survey galaxies selected from *IRAS* (Dunne et al. 2000) and optical (Vlahakis, Dunne & Eales 2005) samples. Yao et al. (2003) measured correlations between nuclear CO emission in the SLUGS $60 \mu\text{m}$ sample and the FIR luminosity (L_{FIR}) and dust mass (M_{dust}), using both CO(1-0) as a *total* molecular gas tracer and CO(3-2) as a *dense* gas tracer. Similar studies were carried out by Gao & Solomon (2004) sampling IR/CO-selected galaxies; and Mao et al. (2010) sampling a range of spirals, starbursts and AGN. Recently, Wilson et al., (2012) studied correlations between molecular gas and the FIR in HI-selected galaxies as part of the JCMT Nearby Galaxies Legacy Survey (NGLS; Wilson et al., 2009), while Corbelli et al., (2012) targeted galaxies in the Virgo cluster, showing that molecular gas is more closely correlated with the submm than with shorter wavelengths. Clemens et al., (2013) studied a sample of 234 local galaxies selected at 545 GHz ($550 \mu\text{m}$) from the *Planck* early release, and demonstrated that dust mass (derived from FIR-mm SEDs) and atomic gas are strongly correlated,

* *Herschel* is an ESA space observatory with science instruments provided by European-led Principal Investigator consortia and with important participation from NASA.

† E-mail: nbourne22@gmail.com

while the relationship between dust mass and SFR depends on dust temperature.

We study a sample selected at $500\ \mu\text{m}$ from the *Herschel* Astrophysical Terahertz Large Area Survey (H-ATLAS; Eales et al., 2010). H-ATLAS covers the largest sky area of any extragalactic submm survey, hence it probes the largest volume of the local Universe in five photometric bands from 100 to $500\ \mu\text{m}$. It is ideal for producing a sample of nearby galaxies selected by their cold dust content. This unique sample can be used to explore the relative correlations between the FIR/submm wavebands and the various gas phases, including diffuse atomic H I and molecular H₂ traced by CO(2–1) and CO(3–2). In this paper we describe the sample selection and data acquisition in Section 2, before analysing the results in Section 3. The implications of the results are discussed in Section 4 and conclusions are summarised in Section 5.

2 DATA

2.1 The sample

The sample was selected from the three equatorial fields of H-ATLAS Phase 1, which are centred at R.A. of approximately 9^{h} , 12^{h} and 14.5^{h} , and Dec. $\sim 0^\circ$, and cover approximately $160\ \text{deg}^2$ in total. The H-ATLAS survey provides PACS (Poglitsch et al., 2010) imaging at 100 and $160\ \mu\text{m}$ and SPIRE (Griffin et al., 2010) imaging at 250 , 350 and $500\ \mu\text{m}$, as described by Ibar et al., (2010) and Pascale et al., (2011). Source extraction and photometry were conducted using the MADX algorithm (S. J. Maddox et al. in prep.) and will be described in an upcoming paper (E. Valiante et al. in prep.); the procedure is also described by Rigby et al., (2011). Optical counterparts in the Sloan Digital Sky Survey Data Release 7 (SDSS; Abazajian et al., 2009) have been identified using the technique described by Smith et al., (2011), including redshifts from the Galaxy and Mass Assembly survey (GAMA; Driver et al., 2011), and will be described in an upcoming paper (N. Bourne et al. in prep.).

The 17 brightest $500\ \mu\text{m}$ sources with redshifts $z < 0.05$, and fluxes $S_{500} > 250\ \text{mJy}$, were selected from the catalogues (see Table 1). In addition to these, the brightest source from the H-ATLAS Science Demonstration Phase (SDP 1), and the two brightest early-type galaxies from SDP (SDP 4 and SDP 15, morphologically classified by Rowlands et al., 2012) were included for comparison. Lenses can potentially contaminate a sample selected at this wavelength (e.g. Negrello et al., 2010), but the blue submm colours in our sample indicate that none are lenses. Only one galaxy (NGC 5713) has a prior CO(3–2) measurement in the literature; this was a single-beam pointing targeting the nucleus (Yao et al. 2003). The galaxy was retained in the sample because the total extended CO flux had not been measured.

2.2 Photometric data

We used H-ATLAS photometry from the catalogues described above. In addition to MADX point-source fluxes, extended sources were measured using elliptical apertures with semimajor axis given by the sum in quadrature of the

optical isophotal radius and 1.6 times the full-width at half-maximum (FWHM) of the beam (c.f. Rigby et al. 2011). We adopted systematic errors of seven per cent on SPIRE fluxes and 10 per cent on PACS fluxes, following the guidance in the Observing Manuals.¹

Flux from extended sources in the PACS maps can be lost due to the high-pass filter (HPF) used in the naive-projection map-making (see Ibar et al. 2010, for further details). Bright sources were masked in the HPF, however many of the sources in the sample have low surface brightness in the PACS maps and hence were not adequately masked. We therefore rejected the $100\ \mu\text{m}$ data for the sample, as well as the $160\ \mu\text{m}$ fluxes of NGC 5705 and UGC 09215, after inspecting the HPF masks in comparison with the extent of $250\ \mu\text{m}$ emission. The sample is covered by FIR all-sky surveys with the *Infrared Astronomical Satellite* (*IRAS*; Neugebauer et al., 1984) and *AKARI* (Murakami et al., 2007). Point-source catalogues from *AKARI* are available at 9 and $18\ \mu\text{m}$ (Ishihara et al., 2010), and at 65 , 90 , 140 and $160\ \mu\text{m}$ (Yamamura et al., 2009). However, since the *AKARI* bands have PSF sizes ranging from 5.6 to $61\ \text{arcsec}$ (FWHM), these measurements will not be representative of the total flux of these galaxies (which are typically $\sim 1\ \text{arcmin}$ across). We therefore obtained additional FIR photometry from *IRAS* at 60 and $100\ \mu\text{m}$; there were an insufficient number of detections at 12 and $25\ \mu\text{m}$ for the purposes of this study. The 60 and $100\ \mu\text{m}$ bands have PSFs with 1.44 and $2.94\ \text{arcmin}$ FWHM respectively (Soifer et al. 1989), which means that several of the galaxies in the sample may be partially resolved by *IRAS*. Hence the point-source fluxes in the Faint Source Catalogue (FSC; Moshir, Kopman & Conrow 1992) are potentially underestimated, and only four of the galaxies have extended flux measurements in the Revised Bright Galaxy Sample (RBGS; Sanders et al. 2003). We therefore measured extended-source fluxes in the raw *IRAS* scans using the Scan Processing and Integration Tool (Scanpi)², following the procedures outlined by Sanders et al. (2003). Results were inspected visually and with reference to the FSC and RBGS. For unresolved sources, the agreement between Scanpi and FSC was within 15 per cent, which is equal to the systematic errors quoted by Soifer et al. (1989). We therefore adopted this fraction as the systematic error on all *IRAS* fluxes.

We extended the photometric coverage to $22\ \mu\text{m}$ using aperture fluxes from the *Wide-Field Infrared Survey Explorer* (*WISE*; Wright et al., 2010), obtained from the NASA/IPAC Infrared Science Archive. The *WISE* elliptical apertures are based on the apertures defined in the 2MASS Extended Source Catalog (Skrutskie et al., 2006), accounting for the PSF of *WISE* (FWHM $12\ \text{arcsec}$ at $22\ \mu\text{m}$). Comparing these apertures with the size of the sources at $250\ \mu\text{m}$ (which has comparable resolution; FWHM $18\ \text{arcsec}$), we found that the apertures of all but five of the sample were sufficient to enclose all of the emission. We discarded the $22\ \mu\text{m}$ data for NGC 5496, NGC 5705 and NGC 5584,

¹ http://herschel.esac.esa.int/Docs/SPIRE/html/spire_om.html;
http://herschel.esac.esa.int/Docs/PACS/html/pacs_om.html

² Scanpi provided by the NASA/IPAC Infrared Science Archive:
<http://scanpiops.ipac.caltech.edu:9000/applications/Scanpi/>

which had apertures that missed substantial amounts of the $250\ \mu\text{m}$ emission, as well as NGC 5713 and UGC 09215, which had no aperture measurements. Following the *WISE* Explanatory Supplement,³ we applied a correction factor of 0.90 to the $22\ \mu\text{m}$ fluxes for a rising (red) SED, and we assumed a calibration uncertainty of six per cent. The photometry measured for the sample are listed in Table 1.

2.3 CO data

We observed galaxies in the sample with the RxA and HARP instruments on the 15m James Clerk Maxwell Telescope (JCMT), between 2011 February and August, using jiggle and grid mapping modes in order to collect emission from the full optical/submm extent of each source. RxA was used to observe the CO(2–1) line at 230.5 GHz (rest frame), with a half-power beam-width (HPBW) of 21 arcsec, while HARP was used to observe CO(3–2) at 345.8 GHz, with a HPBW of 14 arcsec. Galaxies were observed for typical integration times of around 20min, obtaining rms noise levels between 40 and 500 mK (T_A^*), which were predicted to obtain 5σ detections of the line in the integrated cube. Two of the largest galaxies (NGC 5746 and NGC 5705) were not observed due to the prohibitively long integration time required to cover them, while a further two (NGC 4030 and UGC 09215) were not observed since they were part of the *Herschel* Reference Survey (HRS; Boselli et al., 2010) CO sample. A global CO(3–2) measurement for NGC 4030 was later obtained from the HRS data set (M. W. L. Smith et al. in prep.) and is included in the analysis in Section 3; the measurement of UGC 09215 was unavailable. The rest of the sample were all observed with either HARP, RxA or both instruments. Data were reduced (including first-order baseline-fitting, despiking and masking of timelines affected by varying baselines and high noise) and converted into cubes using the STARLINK software library,⁴ and following the ACSIS cookbook⁵.

We measured the global flux from the entire emitting region of each source by integrating the data cubes along the spectral axis between the expected line edges (i.e. across the full-width at zero intensity, FWZI), and in the spatial pixels within an elliptical aperture. Initial estimates of the line widths were based on the H α 21 cm line measured in the HIPASS cubes (see Section 2.4) and on ancillary CO data where available from the literature. These estimates were also informed by additional CO(1–0) line widths measured in spectra obtained from a companion observing program on the Nobeyama Radio Observatory (NRO; PI: L. Leeuw). These data will be described in an upcoming publication by L. Leeuw et al. (in prep.). We subtracted second-order baselines, smoothed the spectra to $60\ \text{km s}^{-1}$ resolution, and measured the FWZI of the lines. Line widths are presented in Table 2. The NRO data are single-beam ($15''$ HPBW) pointings of the central regions of the galaxies, hence the intensity enclosed may not be the total emission from the galaxy, and it is likely that the CO(2–1) and CO(3–2) lines integrated over the entire galaxy are broader.

The axis ratio and orientation of the elliptical apertures were based on profile fits to the $250\ \mu\text{m}$ images (which have a similar beam size to the CO maps). Since the distribution of (dense) molecular gas does not directly trace that of either the dust or the stars, the size of the emitting region cannot necessarily be inferred from the extent of the submm or optical images. We therefore used a range of aperture sizes to plot a curve of growth for each source, i.e. the cumulative aperture flux as a function of semimajor axis (a), in order to determine the optimal size of aperture in which to integrate the flux. Having done this, the line widths were revised where necessary using the FWZI of the integrated spectrum within the aperture, and curves-of-growth were re-measured using the new line widths until consistent results were obtained. Errors were then calculated by integrating within the chosen aperture on a variance map, in which the variance of each pixel is calculated from the wings of the baseline-subtracted spectrum, masking out the expected velocity range of any emission, and adding in quadrature the uncertainty on the baseline subtraction. This latter was estimated from the covariance matrix of the polynomial coefficients from the baseline fit. Where no detection was obtained at 2.5σ confidence, we calculated 3σ upper limits from the error in an aperture equal to the optical size, making the assumption that the distribution of molecular gas is unlikely to extend beyond the optical disk.

Curves of growth and spectra for the galaxies that were observed are shown in Figure 1. Some of the cubes produced fluctuating curves of growth as a result of poor baseline subtraction. The worst of these is NGC 5584, which has low surface brightness and is extended across the full HARP footprint. The HARP cube appears to contain emission coincident with the spiral arms and within the velocity range of literature CO and H α detections, but the cumulative flux falls in larger apertures due to residual baselines that could not be adequately subtracted with a first or second order fit. As a result it is impossible to be sure whether the flux measured is over- or underestimated, hence this measurement was excluded from the analysis. The curves of growth for CGCG 018-077 and SDP 1 show similar fluctuations outside of the error bars due to residual baselines at high radii, but these are restricted to pixels outside of the optical and submm emission regions, and visual inspection of the cubes indicates that the baselines in the centre have been adequately subtracted so that the aperture measurements used are reliable.

The CO measurements are summarised in Table 2, and are compared to CO line widths from the literature and the H α widths measured in Section 2.4. Literature CO line widths and those from the NRO data set are often smaller than those in the HARP and RxA cubes because they are single-beam measurements containing only the nucleus. H α line widths can differ in general because they trace a different gas phase (which is generally more extended), although in the case of NGC 5713 and NGC 5719 the H α lines are blended.

2.4 HI data

Most of the objects in the sample have H α 21 cm line detections in the literature. Data from many surveys are collected from the HyperLEDA database (Paturel et al. 2003), which

³ <http://wise2.ipac.caltech.edu/docs/release/allsky/expsup/>

⁴ <http://starlink.jach.hawaii.edu/starlink>

⁵ http://www.jach.hawaii.edu/JCMT/spectral_line/data_reduction/acsis/

Table 1: The CO sample, sorted by 500 μm flux, with the H-ATLAS Phase 1 IDs, NED identifiers and J2000 coordinates, B-band D_{25} isophote (arcmin) from HyperLEDA, and FIR/submm photometry in Jy.

H-ATLAS ID	NED ID	R.A.	Dec.	Redshift	D_{25}	S_{22}	S_{60}	S_{100}	S_{160}	S_{250}	S_{350}	S_{500}
J120023.7-010553	NGC 4030	12:00:24	−01:06:00	0.004887	3.8	1.582 ± 0.096	20.88 ± 3.13	45.87 ± 6.88	60.53 ± 6.05	33.79 ± 2.37	14.54 ± 1.02	5.00 ± 0.35
J144455.9+015719	NGC 5746	14:44:56	+01:57:18	0.005751	7.2	0.397 ± 0.025	2.31 ± 0.35	10.37 ± 1.56	24.45 ± 2.45	17.81 ± 1.25	8.82 ± 0.63	3.49 ± 0.26
J144011.1-001725	NGC 5713	14:40:12	−00:17:20	0.006334	2.5	–	23.74 ± 3.56	36.55 ± 5.49	36.48 ± 3.65	15.64 ± 1.10	6.34 ± 0.45	2.05 ± 0.15
J143740.9+021729	NGC 5690	14:37:41	+02:17:27	0.005847	3.2	0.527 ± 0.032	5.99 ± 0.90	16.07 ± 2.41	20.85 ± 2.09	11.31 ± 0.79	5.16 ± 0.37	1.96 ± 0.15
J144056.2-001906	NGC 5719	14:40:56	−00:19:06	0.005781	3.1	0.569 ± 0.034	8.76 ± 1.31	17.68 ± 2.66	19.04 ± 1.90	10.00 ± 0.71	4.70 ± 0.35	1.68 ± 0.14
J142223.4-002313	NGC 5584	14:22:24	−00:23:16	0.005464	3.1	–	2.32 ± 0.35	5.28 ± 0.83	8.29 ± 0.84	5.69 ± 0.40	3.18 ± 0.23	1.30 ± 0.10
J144424.3+014046	NGC 5740	14:44:24	+01:40:47	0.005243	2.7	0.261 ± 0.016	2.98 ± 0.45	6.68 ± 1.03	7.77 ± 0.07	4.91 ± 0.35	2.34 ± 0.17	0.89 ± 0.07
J143949.5-004305	NGC 5705	14:39:50	−00:43:07	0.005864	1.3	–	0.50 ± 0.10	1.42 ± 0.33	–	1.74 ± 0.13	1.20 ± 0.10	0.61 ± 0.06
J142327.2+014335	UGC 09215	14:23:27	+01:43:35	0.004660	2.1	–	1.51 ± 0.23	2.95 ± 0.46	–	2.13 ± 0.16	1.32 ± 0.10	0.53 ± 0.05
J141137.7-010928	NGC 5496	14:11:38	−01:09:33	0.005140	2.7	–	0.89 ± 0.14	2.08 ± 0.37	2.86 ± 0.29	2.55 ± 0.19	1.50 ± 0.13	0.71 ± 0.07
J144611.2-001324	NGC 5750	14:46:11	−00:13:23	0.005627	2.7	0.052 ± 0.004	0.62 ± 0.11	2.40 ± 0.38	3.85 ± 0.07	2.59 ± 0.18	1.26 ± 0.09	0.46 ± 0.04
J143753.3-002354	NGC 5691	14:37:53	−00:23:56	0.006238	1.9	0.239 ± 0.014	3.72 ± 0.56	6.61 ± 1.02	6.35 ± 0.06	2.92 ± 0.21	1.25 ± 0.09	0.46 ± 0.04
J115705.9+010732	CGCG 013-010	11:57:06	+01:07:32	0.039503	0.81	0.104 ± 0.006	3.14 ± 0.47	7.12 ± 1.08	6.38 ± 0.64	2.87 ± 0.21	1.15 ± 0.09	0.40 ± 0.04
J114923.8-010501	NGC 3907B	11:49:24	−01:05:02	0.020774	1.5	0.060 ± 0.004	0.70 ± 0.11	2.18 ± 0.35	2.67 ± 0.27	1.80 ± 0.13	0.81 ± 0.07	0.29 ± 0.03
J141215.6-003759	CGCG 018-010	14:12:16	−00:37:59	0.025596	0.75	0.070 ± 0.004	1.30 ± 0.20	3.29 ± 0.53	3.80 ± 0.05	1.99 ± 0.14	0.82 ± 0.06	0.29 ± 0.03
J140808.5-014208	NGC 5478	14:08:09	−01:42:08	0.025147	0.97	0.053 ± 0.003	0.69 ± 0.13	1.80 ± 0.39	2.65 ± 0.27	1.76 ± 0.13	0.76 ± 0.06	0.26 ± 0.03
–	NGC 2861	09:23:37	+02:08:11	0.016965	1.3	0.056 ± 0.004	0.76 ± 0.12	2.13 ± 0.38	3.26 ± 0.33	1.90 ± 0.13	0.73 ± 0.05	0.25 ± 0.02
J090401.1+012729 (SDP 1)	2MASX- J090401+012729	09:04:01	+01:27:29	0.053439	0.54	0.075 ± 0.005	2.76 ± 0.42	4.36 ± 0.67	3.84 ± 0.05	1.61 ± 0.12	0.61 ± 0.04	0.19 ± 0.02
J090917.0-010959 (SDP 4)	CGCG 006-008	09:09:17	−01:09:59	0.027489	0.95	0.028 ± 0.002	0.54 ± 0.09	1.51 ± 0.27	1.34 ± 0.05	0.69 ± 0.05	0.28 ± 0.03	0.10 ± 0.02
J091205.8+002655 (SDP 15)	2MASX- J091205+002656	09:12:06	+00:26:56	0.054493	0.31	0.068 ± 0.004	0.80 ± 0.13	1.19 ± 0.24	0.90 ± 0.03	0.36 ± 0.03	0.14 ± 0.01	0.06 ± 0.01

Notes: Fluxes in Jy are from WISE (22 μm), IRAS (60, 100 μm), PACS (160 μm) and SPIRE (250, 350, 500 μm) as described in the text. Galaxies down to, and including, NGC 2861 constitute a complete sample of $z < 0.05$ galaxies with $S_{500} > 250$ mJy in the Phase 1 fields. NGC 2861 is on the edge of the 12^h field and does not have an H-ATLAS ID because it is outside of the mask used for source extraction. SPIRE coverage this close to the edge of the map is shallower than elsewhere but is sufficient for imaging this bright source.

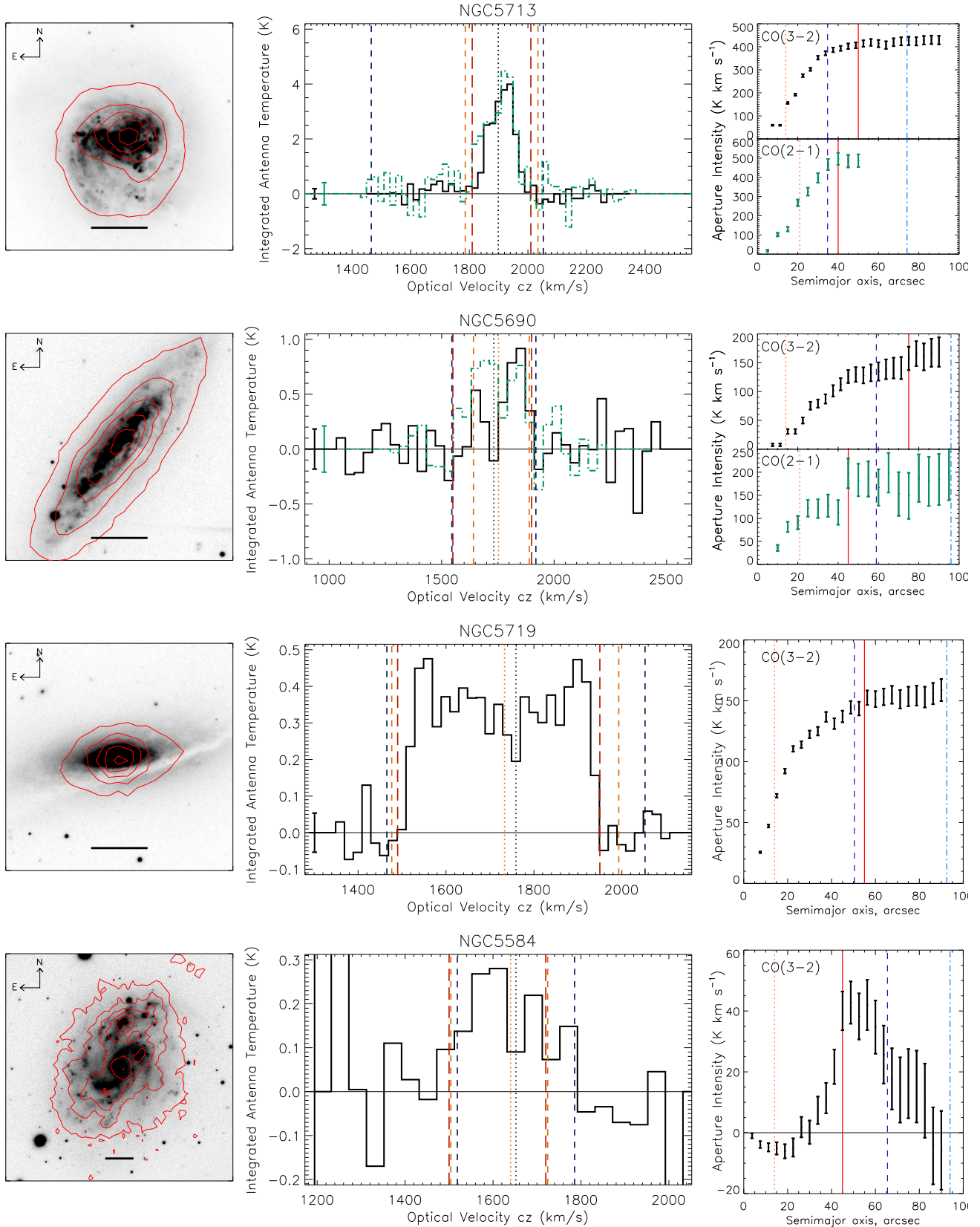


Figure 1. *Left:* SDSS *r*-band images ($2' \times 2'$) with $250 \mu\text{m}$ contours at the 10th, 30th, 50th, 70th, & 90th percentiles. The horizontal black bar in each image is $30''$ in length. *Middle:* aperture-integrated spectra in HARP (black) and RxA (green); blue lines = H I line width from HIPASS; orange = CO line width from literature; red = CO width integrated over for moment maps. *Right:* curves of growth showing integrated intensity as a function of aperture semimajor axis; blue dot-dashed line = semimajor axis of B-band d_{25} isophote; orange dotted line = FWHM of HARP/RxA beam; violet dashed line = $250 \mu\text{m}$ HWHM along major axis; red solid line = aperture chosen to enclose all CO emission. SDP 4 and SDP 15 were observed as single pointings so there is no curve of growth. The anomalous curve-of-growth of NGC 5584 is discussed in Section 2.3. © 0000 RAS, MNRAS 000, 000–000

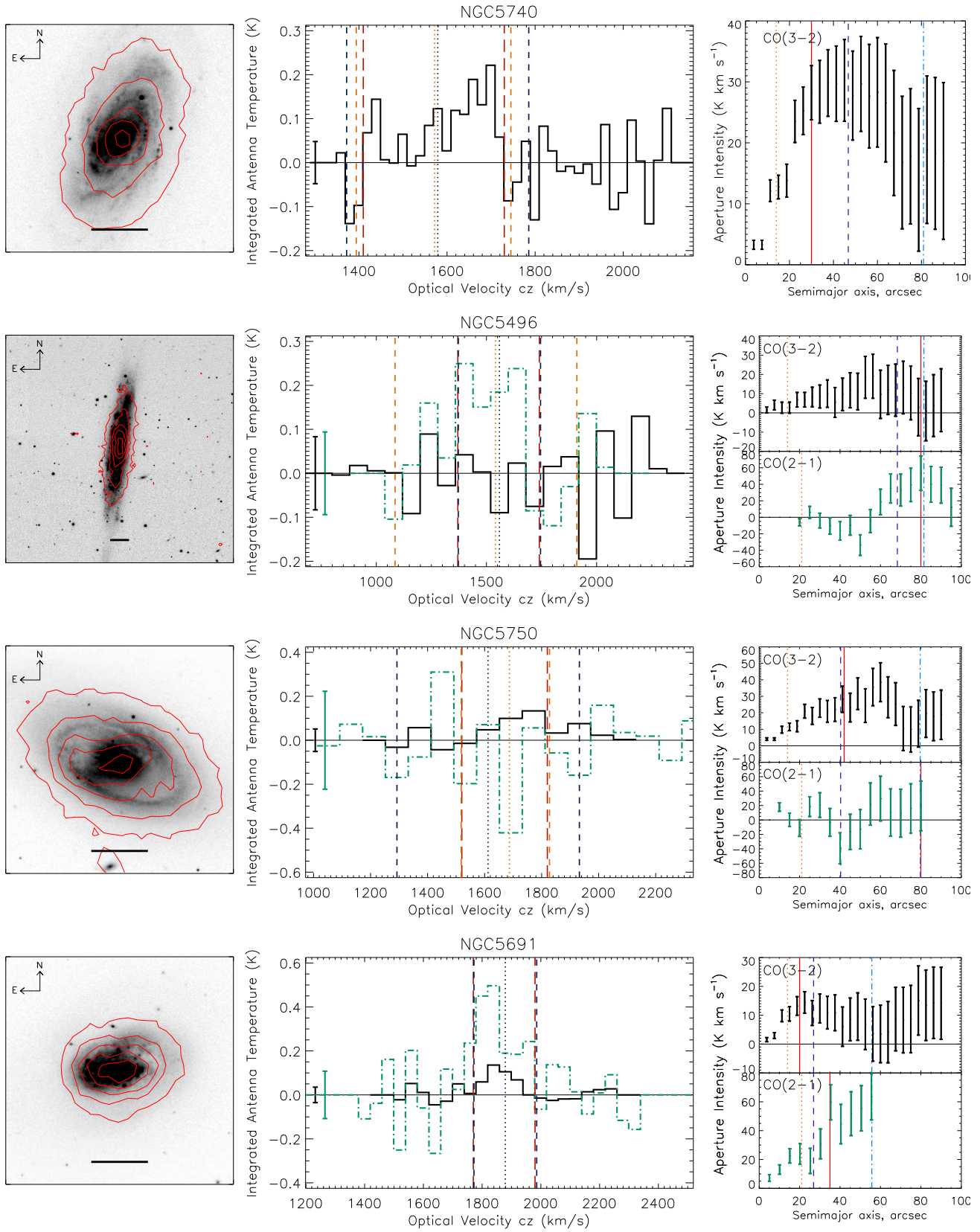


Figure 1. (continued)

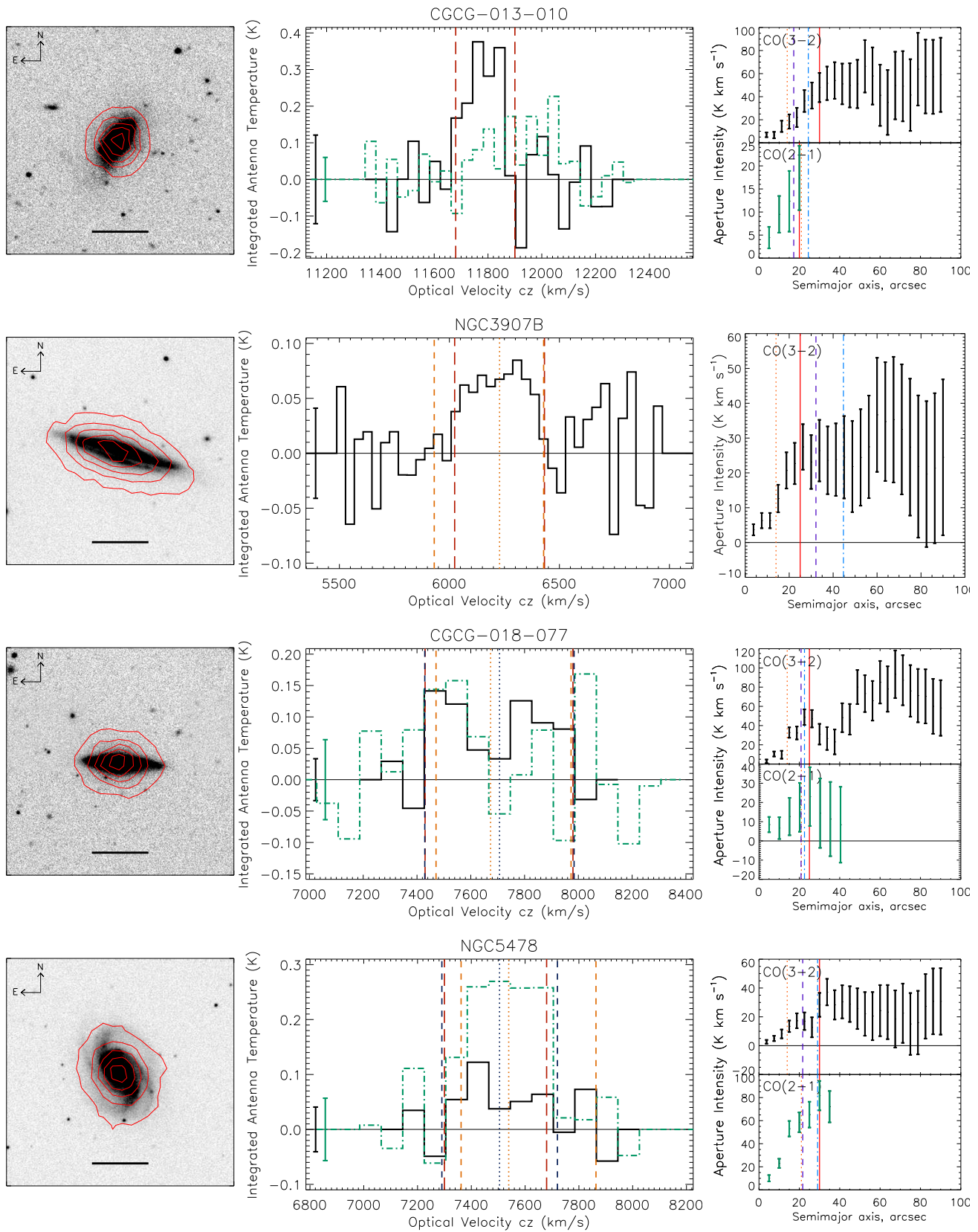


Figure 1. (continued)

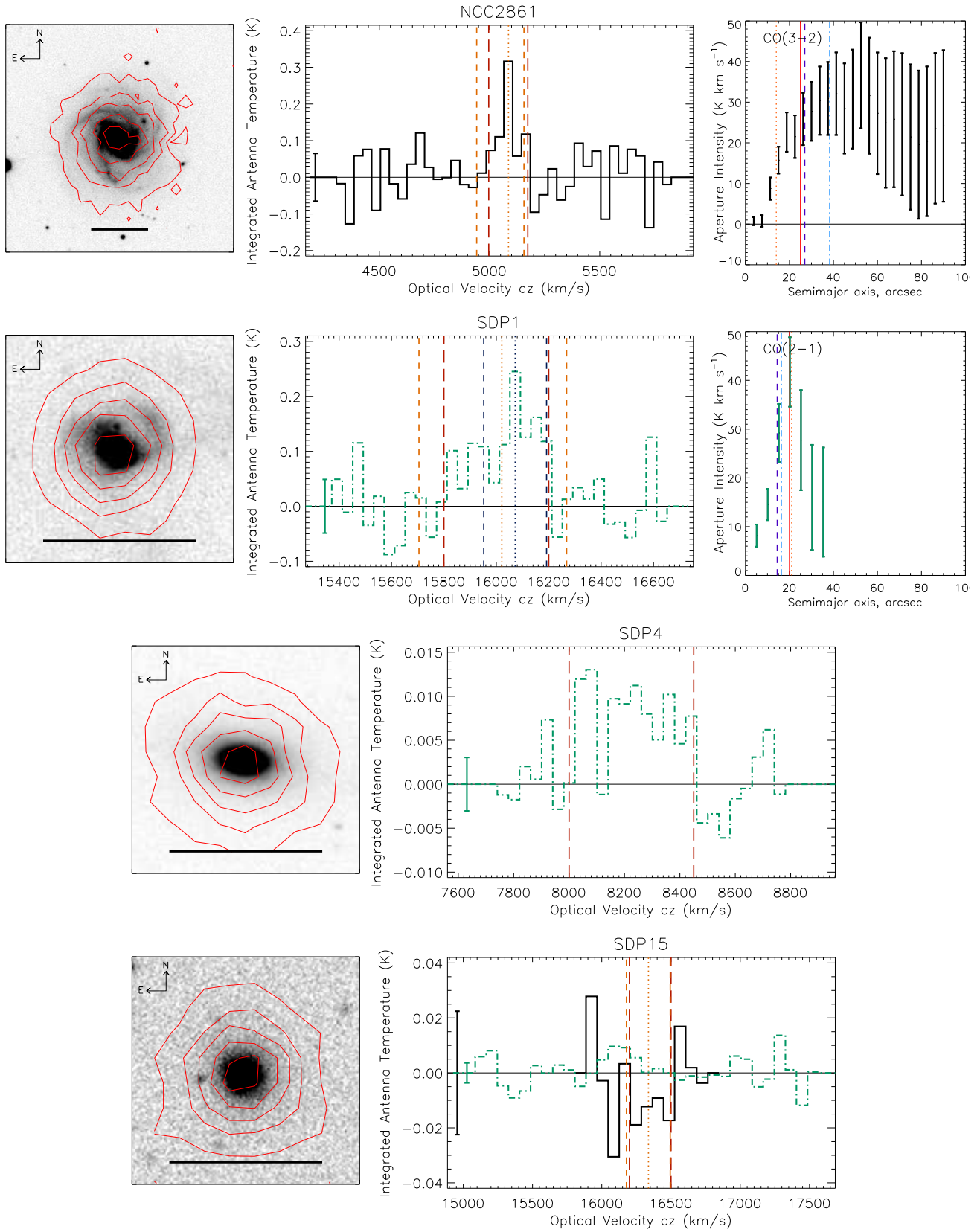


Figure 1. (continued)

Table 2: Details of the CO line measurements including FWZI line widths from literature data (see notes) and from our integrated data-cubes; elliptical aperture axis ratio (a/b) and position angle; semimajor axis, total intensity (or 3σ limit) and signal-to-noise ratio of each line determined from curves of growth.

Galaxy	cz^a	Line width (FWZI, km s^{-1})			Aperture		HARP cube CO(3–2)			RxA cube CO(2–1)			Line ratio I_{32}/I_{21}	
		HI ^b	CO(1–0) ^c	Lit. ^d	Cube	a/b	P.A. ° E of N	a_{32} "	I_{32} $\text{K km s}^{-1} (T_A^*)$	SNR	a_{21} "	I_{21} $\text{K km s}^{-1} (T_A^*)$		SNR
NGC 4030	1465	413	474	360 ¹		1.2	33	53	490.3 ± 33.0^e	14.9				
NGC 5746	1723	633 ^L	227			8.5	170							
NGC 5713	1899	390 ^B	248	140 ²	200	1.0	27	50	405.2 ± 13.1	30.8	40	496.2 ± 31.4	15.8	0.82 ± 0.07
NGC 5690	1732	374	247	243 ³	350	2.7	144	75	157.4 ± 20.3	7.8	45	197.3 ± 32.2	6.1	0.80 ± 0.21
NGC 5719	1756	660 ^B	516	400 ⁴	460	2.3	112	55	149.3 ± 5.9	25.4				
NGC 5584	1652	267	165	136 ⁵	220	1.6	149	45	40.0 ± 6.4	6.3				
NGC 5740	1579	413	350		320	1.7	163	30	28.2 ± 4.4	6.4				
NGC 5705	1732	320				1.5	47							
UGC 09215	1313	466				1.7	162							
NGC 5496	1559	373			370	3.8	173	80	<44.7		80	53.5 ± 20.9	2.6	<0.83
NGC 5750	1612	640	309		600	1.6	71	42	44.0 ± 12.3	3.6	80	<141.6		>0.31
NGC 5691	1879	214			210	1.3	101	20	14.3 ± 3.4	4.2	35	59.7 ± 12.2	4.9	0.24 ± 0.31
C 013-010	11843				220	2.0	144	30	47.9 ± 12.7	3.8	20	17.4 ± 7.0	2.5	2.76 ± 0.48
NGC 3907B	6228	408 ^L	497		400	2.2	72	25	25.8 ± 6.4	4.1	0			
C 018-077	7707	550	502		550	3.1	87	25	47.2 ± 9.1	5.2	25	<45.9		>1.03
NGC 5478	7505	430	501		380	1.2	19	30	28.3 ± 8.3	3.4	30	81.7 ± 12.8	6.4	0.35 ± 0.33
NGC 2861	5085		214		180	1.1	165	25	24.5 ± 6.2	3.9				
SDP 1	16072	240 ^L	563		400	1.3	45				20	45.4 ± 6.8	6.7	
SDP 4	8281				450	1.1	79				0	3.6 ± 0.5	8.0	
SDP 15	16326		316			1.1	20	30	<11.1		0	<1.8		

Notes: (a) Radial velocities (cz , km s^{-1}) are the centre of the HI line and agree with the centre of the CO line in HARP and RxA. (b) HI data labelled (L) are from HyperLEDA, and (B) from the HIPASS BGS (Koribalski et al., 2004); otherwise they are from the HIPASS cubes – see Section 2.4. (c) References for literature data: (1) Young et al. (1995); M.W.L. Smith et al. in prep. (2) Young et al. (1995); Yao et al. (2003); Albrecht, Krügel & Chini (2007). (3) Sauty et al., (2003). (4) Albrecht et al. (2007). (5) Sauty et al. (2003); Böker, Lisenfeld & Schinnerer (2003). (d) CO(3–2) measurement for NGC 4030 from the HRS data (Matthew W. L. Smith, private communication). Missing CO intensities from HARP and RxA indicate sources that were not observed for the reasons described in Section 2.3.

lists HI magnitudes for 15 galaxies in the sample. In addition, many members of the sample have been covered by the HI Parkes All-Sky Survey (HIPASS; Barnes et al., 2001). The HIPASS tables were searched using the Vizier catalogue server⁶, revealing two matches in the HIPASS Bright Galaxy Catalogue (BGC; Koribalski et al. 2004), seven in the main HIPASS catalogue (HICAT; Meyer et al., 2004), and one in the Northern HIPASS catalogue (NHIPASS; Wong et al., 2006). Data are shown in Table 3.

Some discrepancies occur between data in the two catalogues. The homogenised photometry in HyperLEDA have been combined from a wide range of sources, and measurements on different telescopes can vary depending on the uncertainty of the absolute flux calibration, whether the source is fully sampled by the telescope beam, and whether nearby galaxies at the same redshift are blended within a single beam. The average HPBW of the Parkes telescope in multi-beam mode (used for HIPASS) is 14.3 arcmin (Barnes et al. 2001), so all sources in the sample are point sources, and some are potentially blended. NGC 5713 is blended with NGC 5719, and NGC 5746 with NGC 5740. NGC 4030 is 16.7 arcmin away from UGC 07000 at the same redshift, but this galaxy is 3 magnitudes fainter in the optical and has an HI flux of 5.9 Jy km s^{-1} in HyperLEDA (6 times fainter than the HyperLEDA flux of NGC 4030), so it will not significantly bias the NGC 4030 measurement.

The best solution to obtain directly comparable results for a sample is to draw data from a single survey, measured on the same telescope at similar times, and reduced and calibrated in a self-similar way. We therefore used HI fluxes from HIPASS where they were available and not blended. For the brightest sources these were available from the catalogues, as shown in Table 3. Additional data for all sources were obtained from the public HIPASS archive via the ATNF HI Gateway⁷. These extend to a maximum radial velocity of $cz = 12,000 \text{ km s}^{-1}$, so the two sources at $z > 0.04$ (SDP 1 and SDP 15) are not covered. We used the MIRIAD software⁸ to measure point-source spectra at the required positions in data cubes downloaded from the server. Baselines were subtracted from the spectra, and lines were measured between the zero-crossing points. In most cases a first-order polynomial baseline was adequate, except for NGC 2861, NGC 5478, and SDP 4 which required fourth-order fits to remove baseline ripples (c.f. Koribalski et al. 2004). Note that this was possible in these spectra, but not in the CO spectra, because the baseline range was wide enough to fit a higher order polynomial. Results are included in Table 3. In general the results obtained from the cubes are similar to those in the HIPASS catalogues, with three notable exceptions. NGC 5713 and NGC 5719 are blended and at the same velocity, so the measured fluxes will depend on the pixels included in the weighted spectrum and on the line range chosen. The flux we have measured between the zero-crossing points is therefore an overestimate in these cases, but the BGC measurements used a smaller velocity range so are likely to be more reliable. The third exception is NGC 4030, which is

not significantly blended or extended, so it is unclear why our measurement misses 20 per cent of the flux reported in HICAT.

To summarise, we used HIPASS catalogue measurements where they were available and not blended, and measured fluxes in the HIPASS cubes for sources not in the catalogues. We used HyperLEDA fluxes for galaxies that were not detected in the cubes or were blended in the Parkes beam. This left two sources (CGCG 013-010 and SDP 4) with only upper limits from the cubes, and one (SDP 15) with no data at all.

2.4.1 HI self-absorption corrections

HI fluxes and masses will be underestimated if there is sufficient optical depth in the line of sight for HI clouds in the source galaxy to absorb emission from those behind them. This optical depth can depend on the inclination of the galaxy, its morphological type, velocity dispersion and the thickness of the HI disk (e.g. Heidmann, Heidmann & de Vaucouleurs 1972), and also on the column density of individual HI clouds (Braun 2012). Some of the galaxies in this sample are highly inclined and all are dust-rich, so the density of gas is likely to be high. It is therefore prudent to consider the possibility of HI self-absorption (and especially the uncertainty that this introduces) which could affect measured correlations between the HI flux and optically thin emission such as the submm.

Various approaches have been used to correct measured fluxes for self-absorption (e.g. Heidmann et al. 1972; Haynes & Giovanelli 1984; Zwaan et al. 1997; Lang et al., 2003), and their predictions can vary significantly. We follow the method of Haynes & Giovanelli (1984), which is an empirical correction based on observations of 1500 galaxies. The correction factor is a function of axis ratio and morphological type, and is given by

$$f_{\text{HI}} = r_i^{-c} \quad (1)$$

where $r_i \equiv \cos i$ is the observed axis ratio, and c varies from -0.02 to 0.16 depending on morphological type t (de Vaucouleurs et al. 1991). Using this formula, and type information from HyperLEDA, we obtained the corrections shown in Table 3. To account for the uncertainty of the correction, we conservatively allow a 100% error on the estimated self-absorbed fraction itself (i.e. a correction of 1.3 has the error ± 0.3 , such that the error bar encompasses a null correction).

3 RESULTS AND ANALYSIS

3.1 Properties of the sample and line ratios

The 500 μm -selected sample consists of a diverse range of galaxy types, shown by the images in Figure 1. The sample is dominated by red, dusty spirals such as NGC 2861, 3907B, 4030, 5478, 5690, 5740, CGCG 013-010, 018-077; but also contains blue low-surface-brightness disks (NGC 5496, 5584, 5691, 5705, UGC 09215), dust-lane early-types (NGC 5719, 5750), and the starburst/LIRG NGC 5713. The additional sources that are not part of the flux-limited sample comprise two further early-types (SDP 4, 15) and another LIRG (SDP 1).

⁶ Vizier hosted by CDS, Strasbourg: <http://vizier.u-strasbg.fr/viz-bin/VizieR>

⁷ ATNF HI Survey Gateway hosted by CSIRO, Australia: <http://www.atnf.csiro.au/research/HI/hipass/>

⁸ Available from <http://carma.astro.umd.edu/miriad/>

Table 3: Compilation of HI line measurements from HyperLEDA, HIPASS catalogues and HIPASS cubes, with self-absorption corrections (see notes below).

Galaxy	HyperLEDA			HIPASS catalogues			HIPASS cubes			Self-absorption correction				Final
	v_{rad}	Δv	S_{HI}	v_{rad}	Δv	S_{HI}	v_{rad}	Δv	S_{HI}	$i(^{\circ})$	t	c	f_{HI}	$S_{\text{HI}}^{\text{corr}}$
NGC 4030	1463	295	37.9 ± 1.6	1465	441	72.0 ± 0.9	1465	413	56.9 ± 1.5	40	4.0 ± 0.2	0.04	1.01 ± 0.01	72.8 ± 7.4
NGC 5746	1723	633	26.3 ± 1.4				1724	721	29.7 ± 1.5	84	3.0 ± 0.3	0.04	1.09 ± 0.09	28.7 ± 3.3
NGC 5713	1899	160	35.8 ± 1.8	1899	390	$48.8 \pm 5.1^{\text{B}}$	1899	587	73.6 ± 1.4	48	4.0 ± 0.3	0.04	1.02 ± 0.02	36.5 ± 4.1
NGC 5690	1753	266	19.88 ± 0.68	1754	398	$25.6 \pm 0.5^{\text{N}}$	1753	374	21.89 ± 0.89	76	5.4 ± 0.5	0.16	1.25 ± 0.25	32.1 ± 7.3
NGC 5719	1732	355	31.7 ± 1.5	1756	660	$68.3 \pm 5.1^{\text{B}}$	1733	587	74.0 ± 1.2	71	2.4 ± 0.6	0.00	1.00 ± 0.00	31.7 ± 3.5
NGC 5584	1638	166	21.76 ± 0.92	1638	280	27.1 ± 0.4	1638	267	25.54 ± 0.62	42	6.0 ± 0.3	0.14	1.04 ± 0.04	28.3 ± 3.1
NGC 5740	1571	308	21.90 ± 0.88	1572	409	33.3 ± 0.5	1572	413	29.63 ± 0.80	55	3.0 ± 0.4	0.04	1.02 ± 0.02	22.3 ± 2.4
NGC 5705	1760	168	18.7 ± 1.2	1758	279	27.9 ± 0.4	1758	320	26.25 ± 0.72	65	6.5 ± 1.1	0.14	1.13 ± 0.13	31.5 ± 4.8
UGC 09215	1389	162	16.3 ± 1.0	1387	296	23.7 ± 0.5	1397	280	21.12 ± 0.57	64	6.4 ± 0.9	0.14	1.12 ± 0.12	26.6 ± 4.0
NGC 5496	1541	212	39.4 ± 1.4	1541	335	60.9 ± 0.5	1541	373	56.72 ± 0.73	82	6.5 ± 0.8	0.14	1.32 ± 0.32	80.3 ± 21.0
NGC 5750	1687	374	5.17 ± 0.30				1687	640	13.8 ± 1.1	66	0.4 ± 0.9	0.00	1.00 ± 0.00	13.8 ± 1.7
NGC 5691	1871	130	7.66 ± 0.28	1881	219	5.5 ± 0.3	1870	213	5.63 ± 0.71	44	1.2 ± 0.6	0.00	1.00 ± 0.00	5.5 ± 0.6
C 013-010	11843						11843	500	<5.07	65	1.5 ± 2.9	$0.00^{+0.04}_{-0.00}$	$1.00^{+0.04}_{-0.00}$	<5.07
NGC 3907B	6252	408	3.28 ± 0.12				6228	500	<5.81	84	3.1 ± 0.4	0.04	1.09 ± 0.09	3.6 ± 1.0
C 018-077	7676						7674	500	5.44 ± 0.93	74	6.0 ± 2.0	$0.14^{+0.02}_{-0.10}$	1.20 ± 0.20	6.5 ± 1.8
NGC 5478	7530						7539	430	6.03 ± 0.78	49	3.6 ± 0.6	0.04	1.02 ± 0.02	6.1 ± 1.0
NGC 2861	5134	120	2.49 ± 0.09				5086	500	<6.22	25	3.7 ± 0.6	0.04	1.00 ± 0.00	2.5 ± 0.3
SDP 1	9174	240	0.53 ± 0.09							42	0.4 ± 5.0	$0.00^{+0.16}_{-0.00}$	$1.00^{+0.05}_{-0.00}$	0.5 ± 0.1
SDP 4	8281						8241	500	<4.82	75	0.1 ± 2.0	0.00	1.00 ± 0.00	<4.82
SDP 15	16326									28	4.5 ± 5.0	$0.04^{+0.12}_{-0.04}$	$1.00^{+0.02}_{-0.00}$	

Notes: All fluxes are Jy km s^{-1} ; the final flux used for analysis is highlighted in boldface. HyperLEDA fluxes are calculated from magnitudes in the database using $\log S_{\text{HI}} = (17.4 - m)/2.5$. HIPASS catalogue fluxes are from HICAT except where marked B (BGC) or N (NHIPASS). Radial velocities (cz , km s^{-1}) from HyperLEDA are taken from the radio measurements (the v_{rad} parameter), while the line width (Δv) is estimated from the maximum velocity of the gas ($v_{\text{maxg}} \times 2$). Velocities from the HIPASS catalogues are given by the v_{50} or $RV50_{\text{max}}$ keywords, and widths are $RV2 - RV1$ (which generally exceeds $v_{\text{maxg}} \times 2$). Fluxes were measured in the HIPASS cubes between the zero-crossing points, and where no line was detected a 5σ upper limit was measured assuming a width of 500 km s^{-1} . Corrections for HI self-absorption (f_{HI}) are given by equation (1), as a function of inclination angle i and de Vaucouleurs type t , following Haynes & Giovanelli (1984). Errors on f_{HI} include both the uncertainty on t (from HyperLEDA) and a 100% uncertainty on the self-absorbed fraction (see text). Errors on the final corrected fluxes ($S_{\text{HI}}^{\text{corr}}$) include the error on f_{HI} as well as measurement errors from on the flux and a 10% calibration error added in quadrature.

Our data, while not reaching sufficient rms to map the emission in most cases, nevertheless demonstrate that emission in CO(3–2) and CO(2–1) is often extended throughout the disk, as can be seen in the rising curves of growth and broad spectra in Figure 1. We detect line emission in either CO(3–2) or CO(2–1) in most of the sample, including three of the four early-type galaxies (NGC 5719, 5750, SDP 4), as shown in Table 2. NGC 5719 is noteworthy since its warped dust lane and counter-rotating gas and stellar disks indicate that dust and gas were accreted from an interaction with NGC 5713 (Vergani et al. 2007; Coccato et al. 2011). Our CO(3–2) moment map shows that rotation of the molecular gas follows that of the counter-rotating disk and is therefore also likely to have been accreted.

Although we only detect both CO lines in five galaxies, a wide range of line ratios ($R_{32} = I_{32}/I_{21}$) is apparent in Table 2, consistent with the diversity of the sample. Similarly broad ranges of $R_{31} = I_{32}/I_{10}$ were reported in the nuclei of SLUGS galaxies by Yao et al. (2003) and in the large sample of nearby galaxies by Mao et al. (2010). In contrast, Wilson et al. (2012) found a relatively small range of R_{32} and R_{31} in global line intensities of the HI-selected NGLS sample, which may suggest that submm selection probes a wider range of star-forming properties than HI selection. The highest detected R_{32} in our sample belongs to CGCG 013-010 ($R_{32} = 2.76 \pm 0.48$), indicating high excitation perhaps by an AGN or nuclear starburst. The CO(2–1) upper limit on CGCG 018-077 also implies a high ratio greater than 1.0. Perhaps surprisingly, the starburst NGC 5713 has a global R_{32} of just 0.82 ± 0.07 , although this is likely to be much higher in the nucleus (Yao et al. 2003, measured a high excitation of $R_{31} = 1.65^{+0.22}_{-0.29}$ in the central $15''$). We measure a similar value of R_{32} in the star-forming spiral NGC 5690, while lower values are measured in NGC 5691 and 5478.

3.2 Correlations between global fluxes

The total CO line intensity in a galaxy is correlated with FIR flux as encapsulated by the SK law, and correlations have also been observed in the submm in low-redshift galaxies (Dunne et al. 2000; Yao et al. 2003; Corbelli et al. 2012; Wilson et al. 2012) and high-redshift SMGs (Greve et al., 2005; Iono et al., 2009; Engel et al., 2010; Ivison et al. 2011; Magdis et al. 2011; Bothwell et al., 2013). The current sample is novel because it was selected from a blind survey of the local Universe at $500 \mu\text{m}$, and is selected primarily on cold dust mass rather than FIR luminosity or SFR. Using our coverage of the IR SED, we can explore the correlation between the integrated line emission and IR fluxes at various wavelengths, comparing the FIR ($\lambda \lesssim 200 \mu\text{m}$) with the submm ($\lambda \gtrsim 200 \mu\text{m}$).

Figure 2 compares the global fluxes in the CO lines to the global fluxes in the IR from 22 to $500 \mu\text{m}$, and to the HI fluxes. The total integrated intensities ($\text{K km s}^{-1} T_A^*$) in Table 2 have been converted to flux in Jy km s^{-1} using

$$S_{\text{CO}} = \frac{2k_B \Omega I_{\text{CO}}}{\eta_{\text{mb}} \lambda^2} \quad (2)$$

(e.g. Rohlfs & Wilson 2006), where η_{mb} is the main-beam efficiency, which is taken to be 0.63 for HARP and 0.69

for RxA.⁹ In this equation, Ω is the solid angle (in steradians) over which the intensity is averaged. For point sources measured in a single beam, this is the beam area, but for extended sources measured in apertures, the relevant solid angle is the pixel area, which is $(7.5 \text{ arcsec})^2$ for HARP and $(10.0 \text{ arcsec})^2$ for RxA maps.

Correlations clearly exist between the fluxes in both CO lines and all IR bands in Figure 2, but there is considerable scatter outside of the error bars, indicating intrinsic variation within the sample. A correlation also exists between CO(3–2) and HI ($p = 0.001$), while CO(2–1) and HI are not significantly correlated, although only six sources have both lines detected. Figure 3 shows the correlations between the HI fluxes and the same IR bands. Scatter is particularly high in the correlation with the *WISE* and *IRAS* bands, but shows a marked reduction as the IR wavelength is increased. Two notable outliers persist through each of the plots in Figure 3, which are SDP 1 (with the lowest HI flux) and NGC 5496 (with the highest). These two are also outliers in the CO–HI correlation (Figure 2, last panel), with SDP 1 having a very high CO(2–1)/HI ratio, and NGC 5496 having low CO(2–1)/HI and CO(3–2)/HI ratios (the latter being an upper limit). These outliers will be revisited in Section 4.3.

3.3 Strength of the correlations

We use the non-parametric Spearman’s rank coefficient r_s to compare the relative strengths of the correlations in Figures 2 and 3. These coefficients, which are printed in the upper left of each panel, are calculated using all detected fluxes (not including upper limits or the uncertain detection of NGC 5584). Alongside the r_s coefficients of each correlation, we also show the associated p -values (one-sided probability of measuring the given correlation strength under the null hypothesis). These indicate that the correlations between all IR bands and CO(3–2) or HI fluxes are significant ($p < 0.05$), but that correlations between FIR bands at $\lambda \leq 160 \mu\text{m}$ and CO(2–1) are not. If we exclude the galaxies which are not part of the flux-limited sample (see Table 1), results are consistent within errors, and the p -values for CO(3–2) and HI correlations remain significant ($p < 0.05$).

The r_s values show an increase in the level of correlation between the IR and CO(3–2) flux as the IR wavelength decreases from 500 to $100 \mu\text{m}$. This indicates that CO(3–2) is more strongly associated with warmer dust, which increasingly dominates the SED at shorter wavelengths. The decreasing trend at $\lambda \geq 100 \mu\text{m}$ is inverted in the correlations with HI fluxes, which show a strong increase in r_s with wavelength. The correlation of IR flux with the CO(2–1) line also shows a general increase in strength with wavelength, indicating that the emission in this line may be more closely related to cold dust, and possibly HI, than the CO(3–2). However, most of the correlations with CO(2–1) are not significant. Weaker correlations between CO(3–2) and the 22 and $60 \mu\text{m}$ bands break the trend that is seen at longer wavelengths, as does the relatively strong correlation

⁹ See the JCMT Guide to Spectral Line Observing: http://www.jach.hawaii.edu/JCMT/spectral_line/

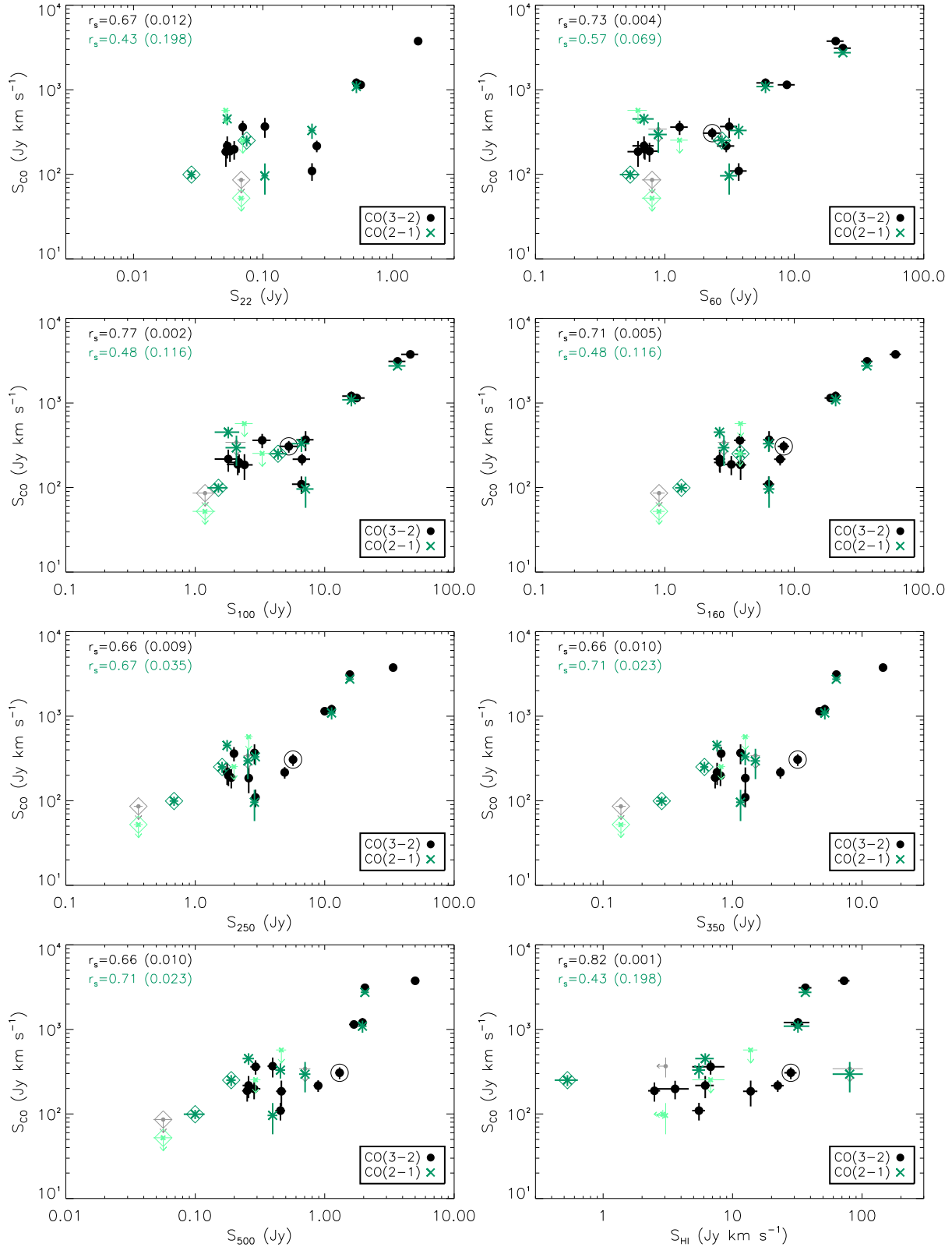


Figure 2. Scatter plots of global fluxes in each of the CO lines as a function of IR fluxes from *WISE* 22 μm , *IRAS* 60, 100 μm , PACS 160 μm , SPIRE 250, 350, 500 μm , and finally HI flux. Data from HARP and RxA are plotted as filled black circles and green crosses respectively. 3σ upper limits on CO and 5σ upper limits on HI fluxes are also shown by arrows in a lighter shade. Large diamonds mark galaxies that are not part of the flux-limited sample (see Table 1). The circled point is the HARP measurement of NGC 5584, which may be inaccurate as described in Section 2.3, and is therefore excluded from the correlation analysis. Spearman's rank correlation coefficients are printed in the top-left corner of each panel, with p -values in parentheses.

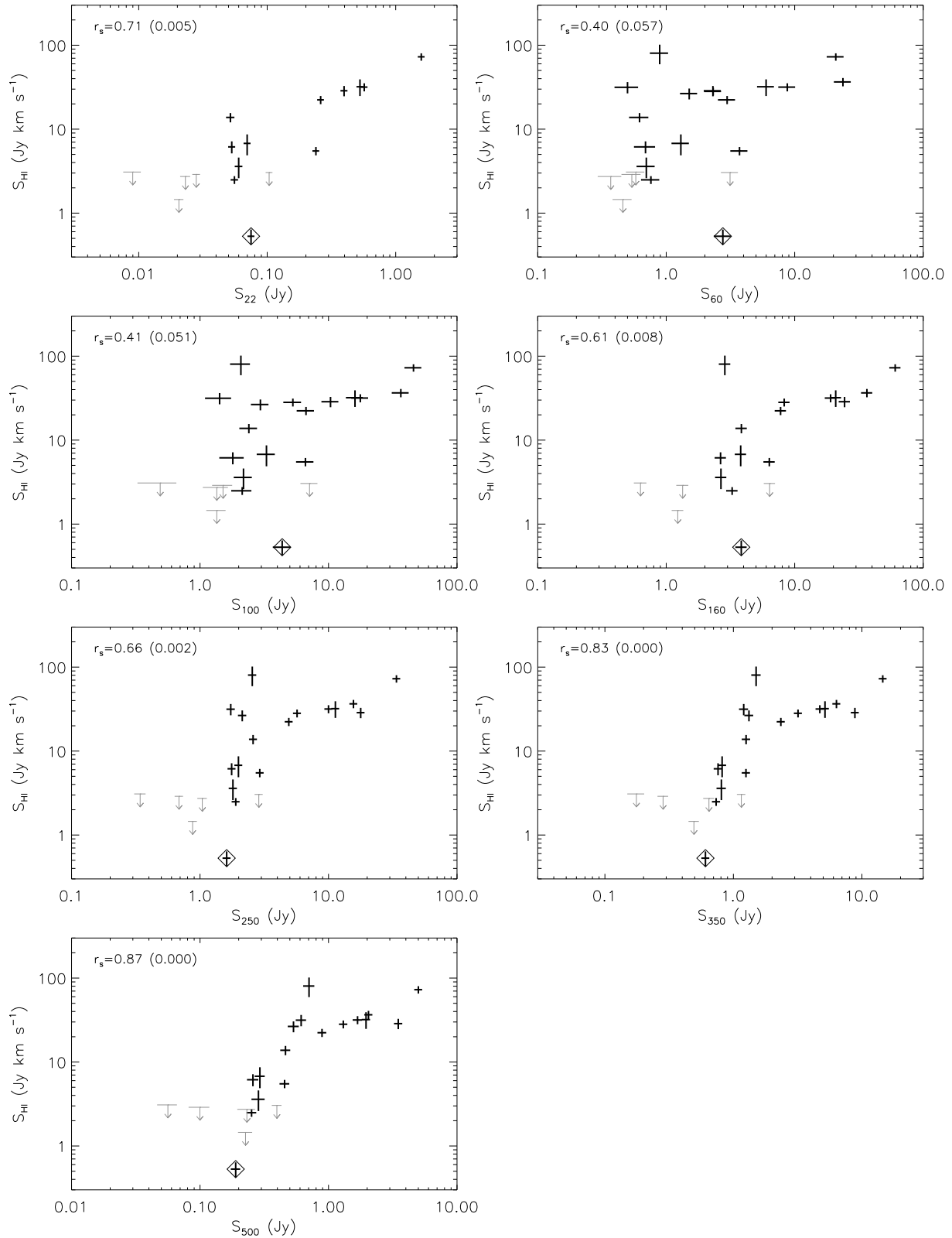


Figure 3. Scatter plots of global fluxes in HI and the IR bands (as in Figure 2). Spearman’s rank correlation coefficients are printed in the top-left corner of each panel, with p -values in parentheses. For galaxies with no flux in the literature and no detection in the HIPASS cubes, 5σ upper limits estimated from the cubes are plotted as thin arrows. The large diamond marks SDP 1, the only galaxy that is not part of the flux-limited sample to have an HI detection.

between HI and $22\ \mu\text{m}$. This may result from a contribution to these wavelengths from stochastically-heated very small grains (VSGs), which may be more strongly associated with cold cirrus dust than warm dust in star-forming regions (Draine & Anderson 1985; Walterbos & Schwering 1987; Xu & Helou 1994; Compiègne et al., 2011).

The trends are visualised in Figure 4 (left-hand panel), in which the uncertainties on r_s are estimated from 500 jackknife resamples of the data, accounting for the potential bias of extreme data points on the measured correlation. We also estimated the uncertainties on the r_s parameters resulting from the flux error bars, by measuring the standard deviation in the measured parameter in 500 Monte Carlo realisations. In each realisation the fluxes were randomly perturbed with a Gaussian probability distribution of width σ equal to the flux error bar. The uncertainty on r_s resulting from the flux errors is on average a factor 2.2 smaller than the uncertainty given by the jackknife method, so we adopted the jackknife errors on r_s as the error bars in Figure 4.

With these uncertainties on r_s it is apparent that the evolution in the HI–IR correlation is significant, but that in the CO(3–2)–IR and CO(2–1)–IR correlations is less so. It is also significant that CO(3–2) is better correlated with $100\ \mu\text{m}$ than either CO(2–1) or HI, and HI is better correlated with the submm (350 and $500\ \mu\text{m}$) than either CO line. The same trends are observed using Pearson’s coefficient r_p and Kendall’s τ parameter as alternative measures of correlation.

3.4 Parameterizing the scatter

In order to understand the intrinsic scatter in the flux correlations we need an estimate of the additional scatter above that expected from the size of the error bars. For this we use χ^2 , which explicitly describes the measured deviation of the data from a given model, in relation to the expected variance due to errors. We measured χ^2 using the FITEXY routine from the NASA IDL library¹⁰, which takes into account errors on both axes following Press et al. (2007). Unlike non-parametric statistics such as Spearman’s rank coefficient, χ^2 depends on the model that the data are compared to, but if the model is plausible then χ^2 is a good measure of intrinsic scatter around that trend. We might expect the various IR bands to be linearly correlated with the gas mass, either as a result of the SK law (assuming the FIR bands trace SFR) or as a result of a constant gas-to-dust ratio (assuming the submm bands trace dust mass). The relationship can vary, however, if these assumptions are not valid, and depending on the linearity of the conversion from the CO tracer to the mass of star-forming gas. We fitted power-laws to the flux scatter plots, weighting by errors on both line fluxes and IR fluxes. Slopes close to unity were obtained in all cases (see Figure 4, right-hand panel), although there is some variation between different lines/bands, which may be genuine or may be biased by outliers in the individual plots.

The χ^2 values of the fits are shown in Figure 4 (middle), with errors estimated from a jackknife resampling of the data. These χ^2 values pertain to the best-fit slopes which

vary between different correlations, but indistinguishable results were obtained using a model with the slope fixed to unity. The χ^2 values increase with IR wavelength from 100 to $500\ \mu\text{m}$ for the CO(3–2) correlations, but decrease for the HI correlations over the same wavelength range. This is consistent with the inverse trends measured in the correlation coefficients. These trends indicate that the CO(3–2) emission, tracing dense molecular gas in star-forming regions, is better correlated with $100\ \mu\text{m}$ fluxes (at the peak of the SED) than fluxes at longer wavelengths (which are increasingly dominated by emission from cold dust). The opposite trend is implied by the HI correlations, and by CO(2–1) between 60 and $250\ \mu\text{m}$ only, suggesting that these two transitions trace different components of the ISM. We will discuss the interpretation of this in Section 4.1.

If we exclude from the analysis the galaxies which are not part of the flux-limited sample (see Table 1), the χ^2 of all correlations with HI are reduced by around a factor 0.6 due to the removal of the outlier SDP 1, but the trend remains the same. Correlations between CO(2–1) and FIR bands with $\lambda \leq 100\ \mu\text{m}$ also have a lower χ^2 due to the removal of SDP 1 and SDP 4, but correlations with longer-wavelength bands are unaffected, and the negative trend with wavelength up to $250\ \mu\text{m}$ remains. Correlations involving CO(3–2) are unaffected because none of these galaxies is detected in this line. Regardless of whether we include all galaxies in the sample, fluxes at $22\ \mu\text{m}$ exhibit less scatter with CO(2–1) and HI than fluxes at 60 – $160\ \mu\text{m}$ (closer to the peak), which suggests that dust emission at $22\ \mu\text{m}$ is more correlated with the diffuse ISM, consistent with the r_s results in Section 3.3.

A more ambiguous observation is that the χ^2 values for the HI–submm correlations imply a similar level of scatter as in the CO(3–2)–submm correlations, while the r_s results imply less scatter in the HI–submm (see black and yellow lines in Figure 4). The χ^2 scales with the number of degrees of freedom: $dof = N_{\text{data}} - N_{\text{model}}$. For the HI–SPIRE correlations, $dof = 17 - 2 = 15$, while for the CO(3–2)–SPIRE correlations, $dof = 12 - 2 = 10$. This relative difference of 1.5 partly explains the discrepancy, but it is also possible that the systematic errors on HI fluxes have been underestimated since the data are from multiple sources, unlike the CO. Under-estimated errors would lead to higher χ^2 overall (since χ^2 measures scatter beyond the errors).

A simple way to quantify the confidence of the trends with wavelength is a linear least-squares fit to the data in the left and middle panels of Figure 4, resulting in an estimate of the slope and its uncertainty (from the jackknife error bars), assuming a linear trend. In fact the trend is unlikely to be linear, since there are multiple dust components whose relative luminosities vary as a function of wavelength according to grain size and temperature (e.g. Draine & Anderson 1985; Compiègne et al. 2011), but in the absence of a more realistic model this is the simplest assumption. We chose to exclude the $22\ \mu\text{m}$ data from these fits since it clearly violates the monotonic trend with wavelength, which we interpret to be a result of the VSG contribution. Assuming that the other bands are dominated by emission from large grains in thermal equilibrium, we can assume that shorter wavelengths trace warm dust, and longer wavelengths trace colder dust. The results of the linear fits are shown in Table 4. Thus, according to the χ^2 results, the correlation of

¹⁰ <http://idlastro.gsfc.nasa.gov/>

Table 4. Confidence levels in slopes of the correlation coefficients and chi-squared with wavelength ($\lambda \geq 60 \mu\text{m}$), from Figure 4.

Line	Parameter	Deviation of slope from zero
CO(3-2)	$r_s(\lambda)$	-1.4σ
CO(3-2)	$\chi^2(\lambda)$	$+3.8\sigma$
CO(2-1)	$r_s(\lambda)$	$+1.5\sigma$
CO(2-1)	$\chi^2(\lambda)$	-0.8σ
HI	$r_s(\lambda)$	$+10.2\sigma$
HI	$\chi^2(\lambda)$	-8.2σ

CO(3-2) with the IR becomes tighter with decreasing wavelength, while both χ^2 and r_s indicate that the correlation of HI with IR becomes tighter with increasing wavelength. The correlation of CO(2-1) with IR may also become tighter with increasing wavelength, but the upturn in χ^2 at 350 and 500 μm reduces our confidence in this observation, while the low significance of the r_s coefficients shows that more data are required to understand this correlation fully.

4 DISCUSSION

4.1 Relationships between ISM tracers

In Section 3 we observed an increase in the scatter between global CO(3-2) and IR flux densities with increasing IR wavelengths ($\lambda \geq 100 \mu\text{m}$), which may indicate that the amount of dense gas (which emits the higher excitation CO lines) is more strongly associated with warm dust (which dominates at $\sim 100 \mu\text{m}$) than cold dust (which dominates at longer wavelengths). This is consistent with the notion of dense gas being the fuel for ongoing star formation, and that star formation is directly traced by emission from warm dust (see Section 4.2). Applying similar arguments to the scatter in the HI/IR [and CO(2-1)/IR] indicates that atomic gas (and more diffuse molecular gas) is more strongly associated with cold dust, although the situation is not clear-cut with CO(2-1) due to insufficient data. In comparison, Corbelli et al. (2012) used the CO(1-0) line to trace the molecular gas content in Virgo spirals with FIR-submm data from the *Herschel* Virgo Cluster Survey (HeViCS Davies et al., 2010). This line traces the total molecular gas mass (modulo uncertainties in the CO/H₂ conversion), and those authors found that it was better correlated with cold dust than warm dust.

Since CO(2-1) tends to be more closely associated with CO(1-0) than CO(3-2) (Israel et al., 1984; Braine et al. 1993; Sakamoto et al. 1995), one would expect correlations involving CO(2-1) to follow the same trends, as is suggested (but not proven) in the current sample. The excitation temperature of CO(2-1) is intermediate between that of the (1-0) and (3-2) lines, so it is not surprising that the results of correlations involving this line are somewhat ambiguous. Nevertheless, the kinetic temperature needed to excite CO(3-2), $T_k \sim E/k_B = 33 \text{ K}$, is about twice that for CO(2-1). Moreover, the critical density required to thermalise the lines is much higher for the (3-2) transition ($n_{\text{crit}} \sim 10^5 \text{ cm}^{-3}$) compared to the (2-1) transition ($n_{\text{crit}} \sim 10^4 \text{ cm}^{-3}$). So it is reasonable to assume that the

CO(3-2) transition traces warm, dense gas in star-forming regions while CO(2-1) traces more diffuse H₂.

There are also parallels in the results of Wilson et al. (2009), who mapped three spirals in the Virgo cluster in CO(3-2) and CO(1-0), and concluded that the CO(3-2) transition was better correlated with two different SFR indicators – 24 μm , tracing warm dust, and H α , tracing ionising radiation from OB stars. Likewise, Iono et al. (2009) and Gao & Solomon (2004) found strong correlations between dense gas tracers [CO(3-2) and HCN respectively] and the FIR, while Wilson et al. (2012) observed a strong CO(3-2)–FIR correlation in low redshift HI-selected galaxies from NGLS. By analogy, Calzetti et al., (2010) showed that the correlation between the FIR and SFR (derived from H α and 24 μm) was shown to have increasing scatter with increasing FIR wavelength (70 to 160 μm) as a result of both variable metallicity and dust heated by old stellar populations.

The scatter in the correlation between CO(3-2) and IR fluxes at $\lambda < 100 \mu\text{m}$ does not follow the trend of the other wavelengths, suggesting that the 22 and 60 μm bands contain some contribution that is not correlated with star formation and dense gas. A likely candidate is emission from VSGs, whose emission spectrum depends on transient heating by individual photons (Draine & Anderson 1985) and can be important at both 22 and 60 μm in low-intensity radiation fields (Compiègne et al. 2011). The incidence of VSG emission varies between different spiral galaxies and may well be better correlated with cold cirrus dust rather than warm dust and SFR (Draine & Anderson 1985; Walterbos & Schwing 1987; Xu & Helou 1994). The relatively low χ^2 and high r_s of the correlation between HI and 22 μm flux indicates that the FIR emission at that wavelength is dominated by dust associated with the diffuse neutral medium. Moving up to 60 and 100 μm , the results in Figure 4 indicate that this contribution weakens relative to dust associated with denser gas.

Considering large grains in thermal equilibrium (which dominate the emission at $\lambda \gtrsim 60 \mu\text{m}$), our results, together with the parallels in the literature described above, constitute strong evidence that dust at different temperatures inhabits different phases of the ISM. Correlations with dense molecular gas tracers such as CO(3-2) and SFR tracers such as H α indicate that warm dust is associated with dense molecular clouds, while correlations with HI [and CO(2-1)] indicate that cold dust is more strongly associated with the diffuse phase of the ISM. It also directly implies that the dominant component of cold dust is less strongly associated with star formation than warm dust, since star formation is fueled by the dense gas. There is a component of cold dust in the cores of dense molecular clouds, where it is shielded from the UV radiation by high optical depths, but the warm dust in those regions dominates the emission. The diffuse ISM is likely to contain a much higher mass of cold dust which dominates the emission at submm wavelengths.

This has implications for the dust heating mechanism. Cold cirrus dust may be heated by the general radiation field, or by UV photons escaping from star-forming molecular clouds (Boulanger & Perault 1988); however, the increased scatter between the submm and both SFR and dense gas suggests that it may be heated by sources other than young OB stars. AGN are a potential source of dust

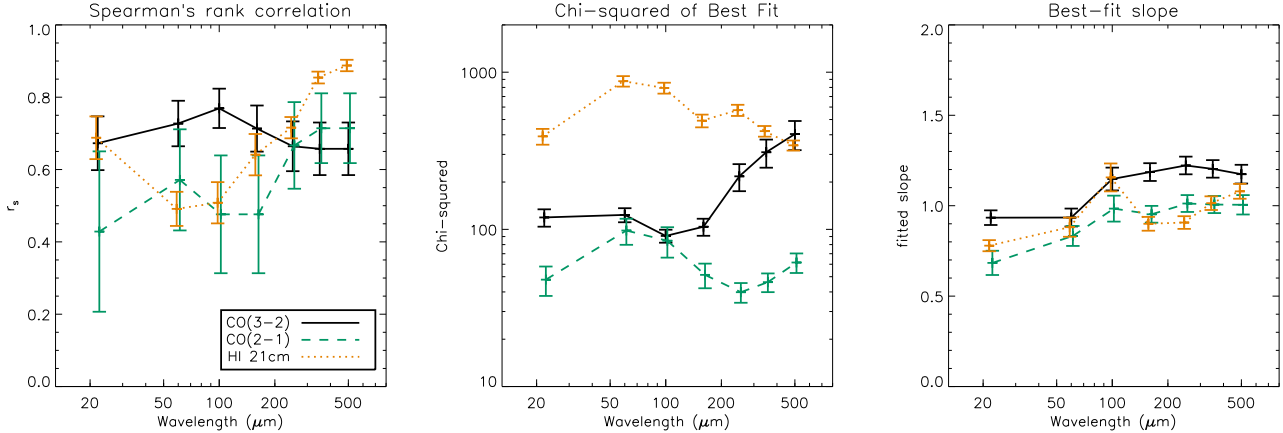


Figure 4. Spearman's rank correlation, χ^2 of the best fit, and slope of the best fit, for the relationship between line fluxes and IR fluxes as a function of IR wavelength. Here, the slope m is defined such that $S_{\text{line}} \propto S_{\text{IR}}^m$.

heating, although evidence suggests that the FIR/submm SEDs of AGN hosts are dominated by dust heated by star formation (Schweitzer et al. 2006; Gallimore et al., 2010; Hatziminaoglou et al., 2010). Bendo et al. (2010a) studied the 70–500 μm SED of the low-luminosity AGN host M81, and found evidence for synchrotron emission from the AGN contributing to the 500 μm flux, but only within the central ~ 2 kpc. The majority of our sample (apart from SDP 1 and SDP 15) have no recorded evidence of an AGN (e.g. in SDSS spectra) so synchrotron emission is unlikely to affect the measured correlations. We tested this by extracting 1.4 GHz fluxes from the NVSS (Condon et al. 1998), using a 30-arcsec matching radius. The radio fluxes appear to be dominated by star formation rather than AGN (see the FIR–radio correlation in Section 4.2). To test whether synchrotron or free-free emission related to star formation could bias the 500 μm fluxes, we assumed a synchrotron spectrum $S_\nu \propto \nu^{-0.8}$, and a free-free spectrum $S_\nu \propto \nu^{-0.1}$ (Condon 1992). Adopting the free-free fraction of 0.76 at 33 GHz (Murphy et al., 2012), we extrapolated from 1.4 GHz to 500 μm and found that the contribution of free-free plus synchrotron emission is less than 2 per cent of the observed 500 μm fluxes, so will have a negligible effect on the correlations.

Having ruled out AGN dust-heating and radio emission affecting the submm–CO correlations, it is likely that the scatter is increased by cold dust being heated at least partially by old stars (e.g. Helou 1986; Walterbos & Greenawalt 1996). There is much observational evidence to support this theory from the correlations between FIR colours and photometric tracers of old and young stars, both in resolved regions within galaxies (Boquien et al. 2011; Komugi et al., 2011; Bendo et al. 2010a, 2012; Groves et al. 2012; Smith et al. 2012b) as well as in the global properties of galaxies (Rowan-Robinson et al., 2010; Totani et al. 2011; Boselli et al., 2012). The high level of scatter in the correlations between dense CO and the long wavelength bands in particular shows that these submm wavelengths do not directly trace SFR, but rather trace diffuse dust (and gas) which may not be associated with star-formation. Even the 100 μm band shows considerable scatter ($r_s = 0.77 \pm 0.06$;

$\chi^2 = 91 \pm 9$) suggesting a significant contribution from cold dust not correlated with the SFR. Reliable IR SFRs can only be obtained from full SED fits to data covering the peak, and allowing for emission from at least two components of dust.

4.2 Infrared SED fitting

We used the six photometric data points to fit a two-component SED model for each galaxy:

$$L_\nu(\nu) = 4\pi \kappa_{850} \left[\left(\frac{\nu}{\nu_{850}} \right)^{\beta_w} M_w B_\nu(\nu, T_w) + \left(\frac{\nu}{\nu_{850}} \right)^{\beta_c} M_c B_\nu(\nu, T_c) \right]. \quad (3)$$

The 22 μm fluxes were treated as upper limits to allow for the possibility of a VSG emission component, over that from the thermal hot dust, which cannot be modelled using modified blackbodies. The dust emissivity term $\kappa_\nu \propto \nu^\beta$ was normalised to $\kappa_{850} = 0.077 \text{ m}^2 \text{ kg}^{-1}$ at $\nu_{850} = c/(850 \mu\text{m})$ (Dunne et al. 2000). Uncertainty in this value leads to a systematic uncertainty in the normalisation of dust masses, but assuming that large dust grains (which dominate at $\lambda \gtrsim 60 \mu\text{m}$) have similar emission properties in different galaxies, the trends observed in the results will be robust. The spectral index of emissivity was fixed at $\beta_c = 2$ for the cold dust component and $\beta_w = 1.5$ for the warm (e.g. Li & Draine 2001; Dale & Helou 2002; da Cunha, Charlot & Elbaz 2008). This parameter depends on distributions of grain size and temperature, which motivates the choice of a higher value for the cold, cirrus dust component; values between 1.5 and 2 are generally measured in external galaxies (see also Dunne & Eales 2001). Using $\beta_c = 2$ for cold dust provides a good fit to nearby galaxies observed with *Herschel* (Davies et al., 2012; Smith et al., 2012c), at least for metal-rich, high surface brightness galaxies (Boselli et al. 2012).

The remaining free parameters are the masses of warm and cold dust, M_w and M_c , and their temperatures, T_w and T_c . We were unable to adequately constrain T_w with the 22 μm data as an upper limit only, but M_c and T_c are well constrained after fixing T_w . Repeating the fitting with T_w

fixed at a range of values between 30 and 60 K, we found that 45 K gave the minimum χ^2 , and so this value was assumed. The potential for a varying β_c leads to a small uncertainty in T_c and M_c ; for example using $\beta_c = 1.5$ leads to a temperature increase by 15 – 30 per cent (2 – 7 K) and a change in mass of up to ± 10 per cent.¹¹ Derived values are collected in Table 5 and the models are shown in Figure 5. Dust temperatures are typical of the full H-ATLAS sample, while luminosities and masses are consistent with the low end of the H-ATLAS sample (Smith et al., 2012a), which is explained by the selection of very nearby galaxies in the current sample. The SEDs do not show any evidence for an additional component of cold dust at $T \sim 10$ K (e.g. Galametz et al. 2011).

We integrated the model SED to obtain $L_{\text{FIR}} = L_{40-120 \mu\text{m}}$, a commonly-used estimate of SFR. This integral is not dependent on the assumed β_w or T_w since the normalisation is constrained by the data at 60 and 100 μm . Similarly, it should not be strongly affected by VSG emission (which can be important at $\lambda \lesssim 60 \mu\text{m}$). We can test the assumption that L_{FIR} traces SFR by comparing to radio continuum luminosities from the NVSS (Condon et al. 1998). We matched to the NVSS catalogue on Vizier using a 30 arcsec matching radius, and found 1.4 GHz fluxes for all but NGC 5705. In Figure 6 we plot the FIR–radio correlation, showing that the FIR luminosities are consistent with the expected correlation for star-forming galaxies from Bell (2003). The tightness of this correlation indicates that the FIR luminosities do not significantly overestimate the SFR assuming that 1.4 GHz is a linear tracer of SFR (in fact it is not quite linear for $L_{1.4} < 6.4 \times 10^{21} \text{ W Hz}^{-1}$ as discussed by Bell (2003), but the deviation is small compared to the errors in this sample).

In Figure 7 we plot our estimate of L_{FIR} against CO luminosity in each of the two emission lines, defined as

$$L_{\text{CO}} = \frac{I_{\text{CO}} \Omega d_L^2}{(1+z)^3} \text{ K km s}^{-1} \text{ pc}^2 \quad (4)$$

where d_L is the luminosity distance in pc. In order to remove the confounding effect of the d^2 factor, which can accentuate correlations between luminosities, we plot the ratio of luminosities against L_{CO} in the right-hand panel of Figure 7. The scatter in these plots confirms that CO(3–2) is better correlated with the integrated FIR than CO(2–1), as was also seen in the flux correlations. The $L_{\text{FIR}}/L_{(3-2)}$ ratio appears to be roughly constant across the sample, although one galaxy is a marginal outlier (NGC 5691, which has the lowest $L_{(3-2)}$ and the highest ratio). This is a very blue spiral

¹¹ We acknowledge the possibility that dust masses measured by fitting global photometry in this way can be biased compared with spatially resolved measurements which separate the dense and diffuse phases of the ISM (e.g. Bendo et al. 2012). For example, global photometry can under-estimate the contribution of the warm component at long wavelengths, leading to an over-estimate of its temperature and an under-estimate of its mass. Although we cannot be sure of the size of this bias using the current data, we note that our excellent photometric coverage of the SED should give reliable constraints on the dust masses under a two-component assumption. As always, absolute values of dust masses should be treated with caution considering the assumptions in the model.

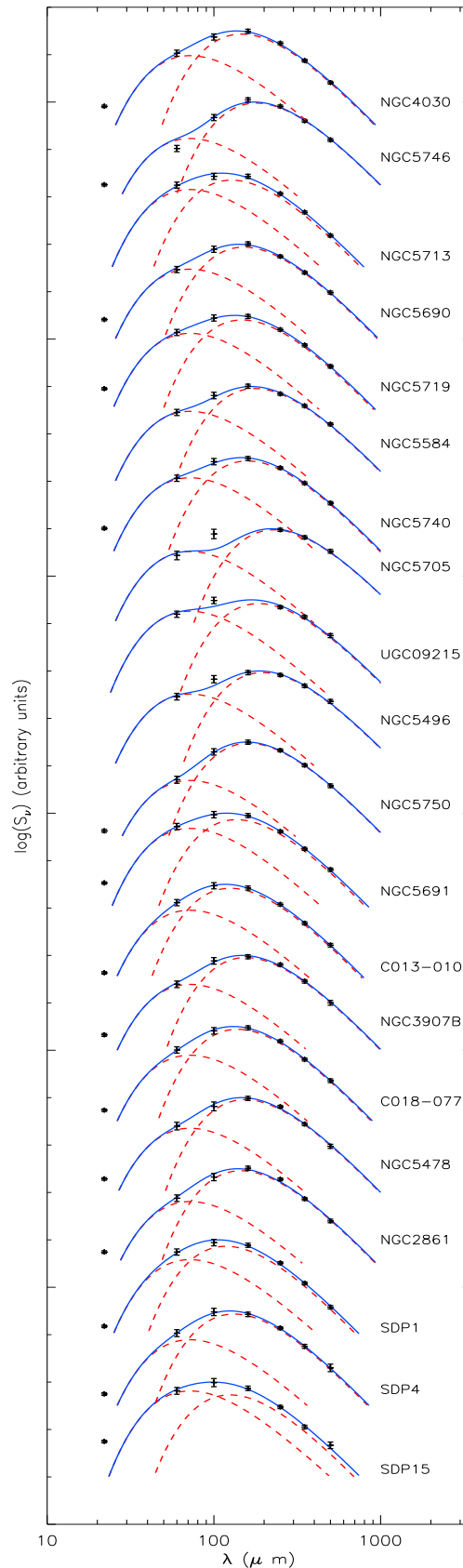


Figure 5. Photometry and best-fit two-component SED models for galaxies in the sample. Note that the 22 μm data were used as upper limits to allow for a contribution from very small grains that cannot be modelled as a modified blackbody.

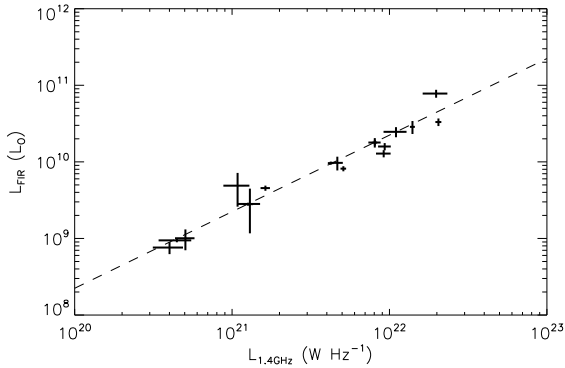


Figure 6. The correlation between integrated 40 – 120 μm FIR and 1.4 GHz radio continuum luminosities. The dashed line is the correlation from Bell (2003).

galaxy which appears to be strongly star-forming; it also has a relatively high M_w/M_c ratio from the SED fit, indicative of a hot SED, so it is possible that the gas excitation conditions are different or that there is another contribution to the integrated L_{FIR} in this source. Figure 7 also shows L_{FIR} against the HI luminosity, in which the correlation is very weak. If L_{FIR} traces the SFR, this indicates a surprisingly weak relationship between the atomic gas reservoir and the SFR, albeit over a relatively small luminosity range. This could be due to a large fraction of the 40 – 120 μm emission arising from dust heated by old stars in this submm-selected sample, or it may be that the galaxies with high FIR/HI ratios have a greater fraction of gas in the molecular phase.

4.3 Dust-to-gas ratio and metallicity

Figure 8 shows the dust mass from the SED models plotted against the CO luminosity and HI mass, as well as the ratios as in Figure 7. Errors on dust mass include a 10 per cent error due to the uncertainty of β (as described above), added in quadrature to the random errors from the SED fit. The HI mass is estimated as

$$M_{\text{HI}} = 2.36 \times 10^{-5} d_L^2 S_{\text{HI}} M_{\odot} \quad (5)$$

(e.g. Dunne et al. 2000). We have not attempted to estimate M_{H_2} due to uncertainties in the CO line ratios and the CO–H₂ conversion (which will be discussed below).

The galaxy with the lowest $M_{\text{dust}}/L_{\text{CO}}$ in both CO lines is NGC 5713, which is atypical of the sample as it is a starburst galaxy from the SLUGS sample. Apart from this outlier, there is very little scatter in the dust/CO ratio, and a decrease in the ratio with increasing luminosity. There are several outliers in the $M_{\text{dust}}/M_{\text{HI}}$ ratios, in particular SDP 1 (with the highest $M_{\text{dust}}/M_{\text{HI}}$) and NGC 5496 (with the lowest). Both of these were also outliers in the CO–HI correlation, and in HI–IR, as discussed in Section 3.2. SDP 1 is a spectroscopically identified AGN, has a disturbed visual morphology (see Figure 1) and a high luminosity ($L_{\text{TIR}} = 4.0 \times 10^{11} L_{\odot}$), hence it is atypical of the sample. It is also possible that the HI self-absorption is underestimated for this source (in which case it should have a lower $M_{\text{dust}}/M_{\text{HI}}$) – the correction in Section 2.4.1 is based on morphology and inclination alone, but this is likely to be

unreliable for mergers. The object with the second-highest $M_{\text{dust}}/M_{\text{HI}}$ is NGC 5746, which is a dust-rich edge-on spiral, and it is possible that the self-absorption correction was underestimated for this galaxy also (NGC 5746 was not observed in CO so we cannot tell whether it is an outlier in $M_{\text{dust}}/L_{\text{CO}}$ as well). NGC 5496, which has the lowest $M_{\text{dust}}/M_{\text{HI}}$, is another edge-on disk galaxy but is very blue and has low surface brightness (unlike NGC 5746 for example). Due to the high inclination, the HI flux has been corrected by a factor of 1.32 for self-absorption; however without this correction this object remains a significant outlier, so it appears to have an intrinsically low dust/gas ratio. Figure 8 shows that it also has a low stellar mass and low metallicity (see also discussion below).

Overall, the scatter in $M_{\text{dust}}/M_{\text{HI}}$ is greater than in $M_{\text{dust}}/L_{\text{CO}}$, while the scatter in $M_{\text{dust}}/L_{(3-2)}$ is lower than that in $M_{\text{dust}}/L_{(2-1)}$. This contrasts with the flux correlations (see r_s in Figure 4), which indicated that the long-wavelength emission from cold dust was better correlated with HI and CO(2–1). The discrepancy is likely to result at least partially from the dependence of derived dust masses on temperature and β , but there are many other factors which affect this correlation. Scatter could be increased if the extent of HI emission probed by the 14.3 arcmin Parkes beam is larger than the aperture within which the submm flux is measured (~ 1 arcmin), so that the HI measurements probe a larger gas reservoir than the dust measurements (see also Devereux & Young 1990). It is also likely that there is a range of line ratios in the sample, and that CO(3–2) and CO(2–1) do not trace H₂ consistently due to a range of excitations.

A range of metallicities in the sample could also influence these correlations, since both dust/gas and CO/H₂ ratios depend on metallicity. Hence the correlation between CO and M_{dust} may be stronger because galaxies with higher metallicities have higher dust and CO fractions for the same gas mass. We can investigate this with independent tracers of the gas-phase metallicity. Spectroscopic measurements from SDSS DR7 are available in the MPA-JHU catalogue (Tremonti et al., 2004), although only five galaxies in the current sample have metallicities in the catalogue since the others were not classified as star-forming. These values are printed in Figure 8 and in Table 5. The Figure also shows stellar masses for the galaxies, derived from $g-i$ photometry following the method proposed by Taylor et al., (2011), as used in the GAMA survey. We used photometry from the publicly-available GAMA DR1 (Hill et al., 2011), except for six low-surface-brightness galaxies (NGC 5496, 5584, 5690, 5705, 5746, and UGC 09215) where visual inspection revealed that the GAMA Kron apertures did not cover the full extent of the disk. For these six, we measured magnitudes in apertures conservatively defined from the SPIRE images. Stellar mass can be used as an approximate tracer of metallicity via the mass–metallicity relation (Tremonti et al. 2004) or the fundamental metallicity relation (FMR; Mannucci et al. 2010). The FMR combines SFR with stellar mass to reduce scatter in the relationship. Figure 9 shows the relationship between stellar mass and metallicities from MPA-JHU and derived from the FMR respectively. For the latter we have estimated SFR from the radio $L_{1.4}$ following Bell (2003). The SFR is divided by a factor 1.6 to convert to the Chabrier (2003) IMF used by

Table 5: Physical parameters of the sample: stellar masses from MAGPHYS SED models; metallicities from MPA-JHU; CO luminosities and HI masses; and dust properties from the two-component SED models.

Galaxy	M_* ($10^{10} M_\odot$)	Z $12+\log(\text{O}/\text{H})$	L_{32} ($10^8 \text{ K km s}^{-1} pc^2$)	L_{21} ($10^8 \text{ K km s}^{-1} pc^2$)	M_{HI} ($10^9 M_\odot$)	M_{dust} ($10^7 M_\odot$)	T_c (K)	M_w/M_c	$L_{8-1000 \mu\text{m}}$ ($10^{10} L_\odot$)
NGC 4030	2.78 ± 0.26		4.45 ± 0.30		7.45 ± 0.75	4.88 ± 0.32	19.8 ± 0.4	$(2.05 \pm 0.16) \times 10^{-2}$	3.02 ± 0.27
NGC 5746	10.4 ± 0.96				3.77 ± 0.43	7.3 ± 2.2	16.2 ± 1.3	$(3.79 \pm 1.35) \times 10^{-3}$	1.13 ± 0.55
NGC 5713	1.53 ± 0.14		6.16 ± 0.20	67.2 ± 4.2	6.24 ± 0.70	2.51 ± 0.22	22.7 ± 1.0	$(7.34 \pm 1.73) \times 10^{-2}$	4.18 ± 0.78
NGC 5690	0.989 ± 0.091		2.04 ± 0.26	4.15 ± 0.67	3.80 ± 0.39	2.75 ± 0.16	19.2 ± 0.4	$(1.71 \pm 0.12) \times 10^{-2}$	1.42 ± 0.11
NGC 5719	2.94 ± 0.27		1.89 ± 0.075		4.60 ± 0.51	2.188 ± 0.064	19.6 ± 0.2	$(2.93 \pm 0.16) \times 10^{-2}$	1.55 ± 0.085
NGC 5584	0.532 ± 0.049	9.01 ± 0.01	0.453 ± 0.072		3.51 ± 0.35	2.15 ± 0.17	16.4 ± 0.4	$(7.60 \pm 0.99) \times 10^{-3}$	0.466 ± 0.054
NGC 5740	0.910 ± 0.084		0.294 ± 0.046		2.61 ± 0.29	1.109 ± 0.047	18.2 ± 0.2	$(1.71 \pm 0.08) \times 10^{-2}$	0.485 ± 0.024
NGC 5705	0.348 ± 0.032				4.16 ± 0.42	2.14 ± 0.80	12.6 ± 1.3	$(2.17 \pm 1.06) \times 10^{-3}$	0.113 ± 0.061
UGC 09215	0.144 ± 0.013	8.68 ± 0.01			2.23 ± 0.28	0.700 ± 0.22	15.6 ± 1.6	$(1.22 \pm 0.47) \times 10^{-2}$	0.171 ± 0.064
NGC 5496	0.269 ± 0.025	8.66 ± 0.05	< 0.45	< 0.10	6.97 ± 0.70	1.24 ± 0.19	14.8 ± 0.6	$(4.79 \pm 1.08) \times 10^{-3}$	0.156 ± 0.032
NGC 5750	2.19 ± 0.20		0.290 ± 0.098	< 2.01	1.89 ± 0.24	0.731 ± 0.027	17.9 ± 0.2	$(5.79 \pm 0.26) \times 10^{-3}$	0.198 ± 0.011
NGC 5691	0.440 ± 0.04		0.211 ± 0.050	1.43 ± 0.29	0.929 ± 0.11	0.573 ± 0.026	21.2 ± 0.4	$(5.40 \pm 0.50) \times 10^{-2}$	0.685 ± 0.065
C 013-010	8.26 ± 0.76		27.2 ± 7.2	< 19.2	< 36.3	19.1 ± 0.47	23.1 ± 0.3	$(4.34 \pm 0.37) \times 10^{-2}$	27.1 ± 1.77
NGC 3907B	4.67 ± 0.043		4.2 ± 1.0		6.36 ± 1.66	5.95 ± 0.50	18.6 ± 0.4	$(1.17 \pm 0.13) \times 10^{-2}$	2.37 ± 0.27
C 018-077	2.37 ± 0.022	9.01 ± 0.03	11.4 ± 2.2	< 18.1	16.6 ± 3.71	7.09 ± 0.38	20.9 ± 0.4	$(2.19 \pm 0.31) \times 10^{-2}$	5.48 ± 0.68
NGC 5478	4.78 ± 0.44	9.24 ± 0.06	6.64 ± 1.9	31.1 ± 4.9	17.1 ± 2.80	8.02 ± 0.81	18.9 ± 0.6	$(1.14 \pm 0.13) \times 10^{-2}$	3.32 ± 0.48
NGC 2861	3.43 ± 0.32		2.65 ± 0.67		3.18 ± 0.34	3.14 ± 0.40	20.0 ± 0.8	$(1.36 \pm 0.21) \times 10^{-2}$	1.73 ± 0.34
SDP 1	3.87 ± 0.36			75 ± 11	7.09 ± 1.39	15.9 ± 1.5	24.5 ± 1.3	$(8.93 \pm 3.14) \times 10^{-2}$	36.3 ± 10.4
SDP 4	2.69 ± 0.25			1.6 ± 0.20	< 16.4	2.51 ± 0.14	21.9 ± 0.4	$(2.79 \pm 0.40) \times 10^{-2}$	2.52 ± 0.30
SDP 15	2.74 ± 0.25		< 11.9	1.3 ± 1.1		4.18 ± 0.55	23.2 ± 1.2	$(1.56 \pm 0.25) \times 10^{-1}$	10.8 ± 1.30

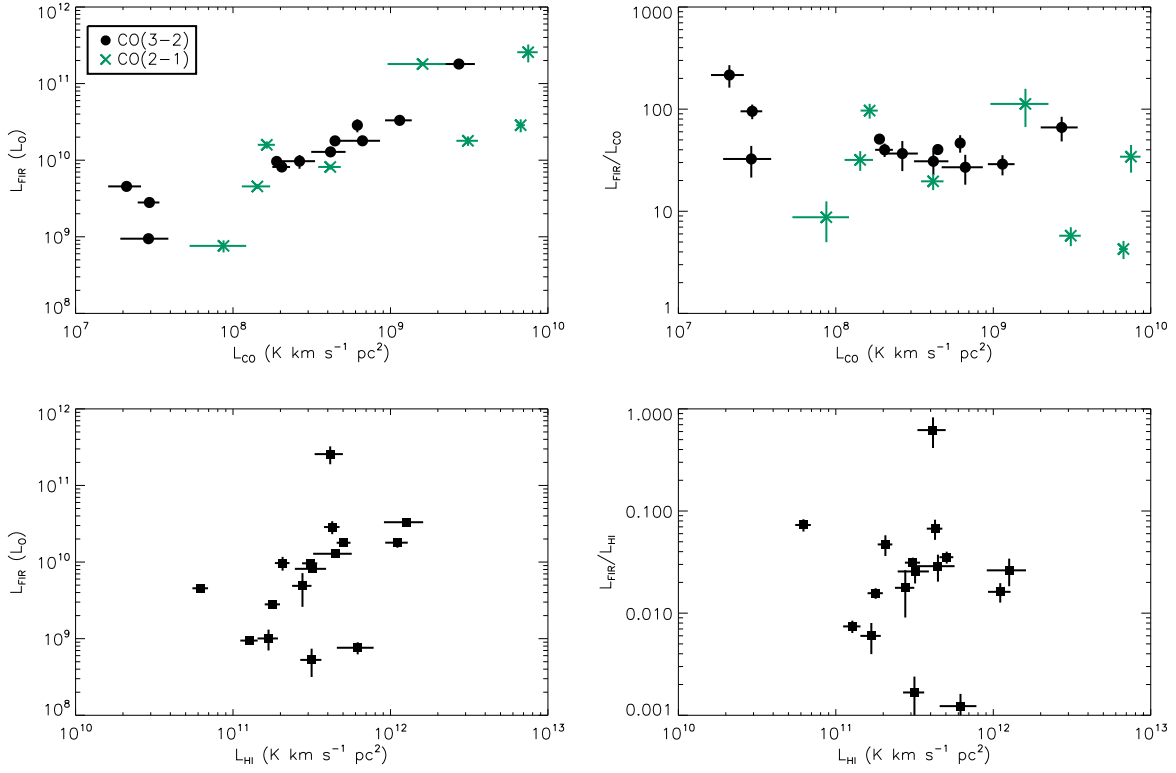


Figure 7. Integrated FIR luminosity L_{FIR} from two-component SED fits versus CO and HI luminosities (left), and the ratios $L_{\text{FIR}}/L_{\text{CO}}$ and $L_{\text{FIR}}/L_{\text{HI}}$ (right).

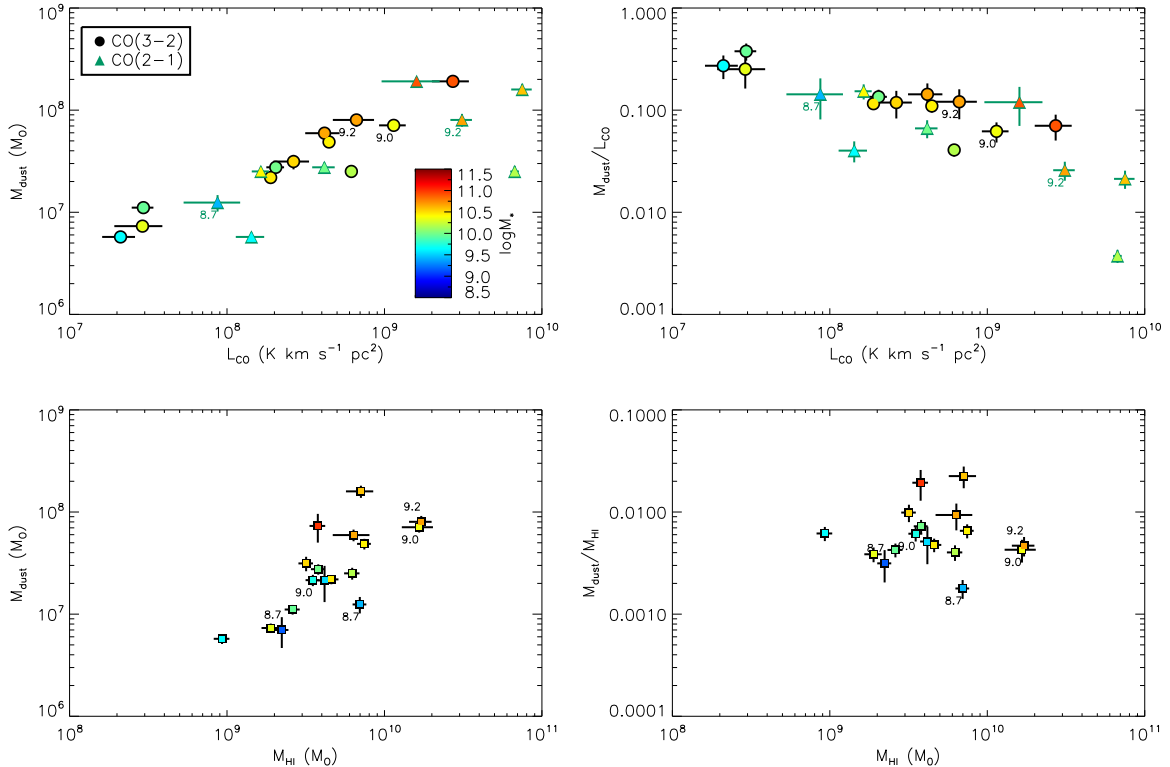


Figure 8. Total dust mass from two-component SED fits versus CO luminosity (top left), and the ratio $M_{\text{dust}}/L_{\text{CO}}$ versus L_{CO} (top right); dust mass versus HI mass (bottom left) and $M_{\text{dust}}/M_{\text{HI}}$ versus M_{HI} (bottom right). Points are coloured according to the stellar mass derived from multiwavelength SED fitting as described in the text. Labels show the metallicities $[12+\log(\text{O}/\text{H})]$ for galaxies with spectroscopic measurements in the MPA-JHU catalogue.

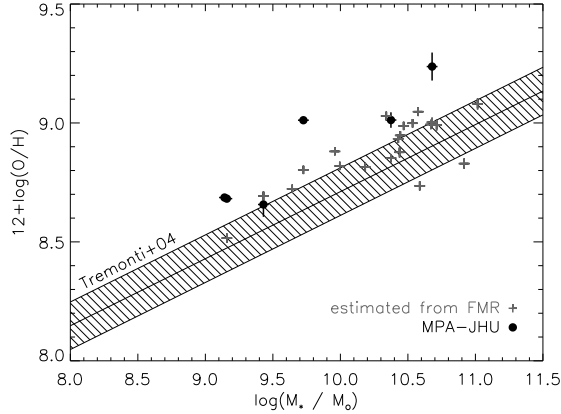


Figure 9. Metallicity estimates from the FMR, based on stellar mass and SFR as described in the text, compared with spectroscopic measurements from the MPA-JHU catalogue. The filled region shows the median $\pm 1\sigma$ scatter of the mass–metallicity relation measured by Tremonti et al. (2004) from SDSS DR7.

Mannucci et al. (2010). Error bars allow for the uncertainty in stellar mass, assuming photometric errors of 0.1mag, and the uncertainty in $L_{1.4}$.

Figure 9 shows that spectroscopically measured metallicities in the sample are systematically high compared with those derived from the FMR for the same galaxies, and compared with the Tremonti et al. (2004) relation. Assuming that the galaxies with spectroscopic measurements are representative of the sample, this could indicate that galaxies in the sample are systematically metal-rich compared with both relations, which is likely considering the selection by dust emission. However, it is also possible that the spectroscopic metallicities are higher because they are measured from SDSS fibres covering the central $\sim 3''$ of the galaxies only, and the metallicity in the disk is likely to be lower (Vila-Costas & Edmunds 1992). Overall, using the stellar masses to estimate the metallicity is subject to large uncertainties due to the complex interplay between stellar mass, SFR and metallicity (Hunt et al., 2012; Lara-López, López-Sánchez & Hopkins 2013), and such estimates are likely to be biased for this sample. Combined with the uncertain conversions from our data to CO(1–0) (note the large range of line ratios in Table 2), and uncertainty in the relationship between CO(1–0)/H₂ and oxygen abundance (Genzel et al. 2012), this will lead to large uncertainties on any estimate of M_{H_2} . Nevertheless, Figure 9 indicates a large range of metallicities, which is likely to increase the scatter in the $M_{\text{dust}}/M_{\text{HI}}$ ratios. A broad metallicity range is supported by the diversity of optical colours and morphologies in the sample, which includes dusty spirals (NGC 2861, 3907B, 5478, 5690, 5740, CGCG 013-010, 018-077); blue low-surface-brightness disks (NGC 5496, 5584, 5691); early-type galaxies (NGC 5719, 5750, SDP 4, 15); as well as the starburst NGC 5713.

4.4 Slope of the CO–FIR relationship

The slope of the relationship between SFR and molecular gas mass, or between their densities (the SK law), is of

interest for understanding how star formation is regulated in galaxies. To measure the slope in the correlations, we fitted power laws to the data in Figure 7. We define the slope n such that $L_{\text{FIR}} \propto L_{\text{CO}}^n$, and we fit $n_{32} = 0.77 \pm 0.10$ ($\chi^2 = 36$) for CO(3–2), and $n_{21} = 0.80 \pm 0.27$ ($\chi^2 = 90$) for CO(2–1). Errors were estimated by increasing the observational errors to give a reduced $\chi^2 = 1$ in the fit, following Tremaine et al., (2002). For reference, Yao et al. (2003) fitted a slope $n_{32} = 1.4$ in their 60 μm -selected SLUGS sample (although they only measured CO in the central 15 arcsec of the galaxies), while Iono et al. (2009) found $n_{32} = 0.93$ for a sample of local and distant IR-selected galaxies covering five orders of magnitude in luminosity. However, the index may vary between different luminosity regimes (e.g. Genzel et al. 2010; Wilson et al. 2012, but see also Ivison et al. 2011), and most of the current sample are not LIRGs (see Figure 7). It may also depend on the CO transition as a result of excitation conditions correlating with luminosity.

Gao & Solomon (2004) fitted a slope of $n_{10} = 1.25$ to the $L_{(1-0)} - L_{\text{FIR}}$ relation in a large sample of nearby galaxies spanning 2.5 orders of magnitude in luminosity, yet a much flatter slope of $n_{10} = n_{32} = 0.87$ was fitted by Mao et al. (2010) to both CO(1–0) and CO(3–2) data spanning over four orders of magnitude. Both of these samples, containing star-forming spirals as well as (U)LIRGs, showed consistent relationships over the full luminosity range. An alternative scenario was presented by Wilson et al. (2012), who analysed a sample of HI-selected galaxies in NGLS and SINGS, in comparison to the LIRG sample of Iono et al. (2009). They split the local galaxies in NGLS into two luminosity ranges and found that galaxies with $8.3 < \log_{10} L_{\text{FIR}} < 9.5$ had systematically higher $L_{\text{FIR}}/L_{(3-2)}$ ratios than $9.5 < \log_{10} L_{\text{FIR}} < 10.7$ galaxies (i.e. $n_{32} < 1$; see Figure 5 of Wilson et al. 2012). This is consistent with the sub-linear correlation seen in the current data. On the other hand, they showed that the LIRGs from Iono et al. (2009) had higher ratios, and fitted a slope $n_{32} \sim 1.2$ for all the galaxies with $\log_{10} L_{\text{FIR}} > 9.5$. The galaxies in the current sample fall in the range $9.1 < \log_{10} L_{\text{FIR}} < 11.6$ (though only SDP 1 and CGCG 013-010 have $\log_{10} L_{\text{FIR}} > 11$) and the mean (standard deviation) of $\log_{10}(L_{\text{FIR}}/L_{(3-2)})$ is 1.7(0.3). This is consistent with galaxies in the same range from Wilson et al. (2012) and significantly lower than the mean for (U)LIRGs and SMGs. Low-redshift submm-selected galaxies therefore appear to be typical of the the normal, disk-mode star-forming sequence, or “main sequence” (Daddi et al. 2010; Genzel et al. 2010). There is clearly some disagreement on the slope of the FIR–CO correlation, with different results being obtained in different samples and in different luminosity ranges. Metallicity is likely to play a role, since the CO/H₂ conversion is sensitive to metallicity (Genzel et al. 2012), and the estimates in Figure 9 indicate a large range of metallicities in the sample.

We define the slope m in the $M_{\text{dust}} \propto L_{\text{CO}}^m$ and $M_{\text{dust}} \propto M_{\text{HI}}^m$ relations, and fit $m_{32} = 0.60 \pm 0.08$ ($\chi^2 = 34$) for CO(3–2), $m_{21} = 0.47 \pm 0.20$ ($\chi^2 = 83$) for CO(2–1), and $m_{\text{HI}} = 0.98 \pm 0.21$ ($\chi^2 = 111$) for HI. Excluding two outliers (SDP 1 and NGC 5496, which may have unreliable self-absorption corrections) from the HI correlation yields $m_{\text{HI}} = 0.97 \pm 0.15$ with $\chi^2 = 48$. Errors were again estimated by increasing the observational errors to give a reduced $\chi^2 = 1$. A linear $M_{\text{dust}}-M_{\text{HI}}$ correlation ($m_{\text{HI}} = 1$) is consistent with

other studies in the literature (e.g. Devereux & Young 1990; Dunne et al. 2000), notwithstanding the scatter in these data. We find the mean ratio of HI gas to total dust mass to be 200 (190 excluding the two outliers), which is similar to that in the SLUGS sample (Dunne et al. 2000). In comparison, Yao et al. (2003) fitted the $M_{\text{dust}}-L_{(3-2)}$ correlation with a slope equivalent to $m_{32} = 1.05 \pm 0.08$ to the SLUGS $60\ \mu\text{m}$ sample. Unlike our two-component fits, Yao et al. used dust masses derived from the $850\ \mu\text{m}$ flux assuming a single temperature fitted to 60, 100 and $850\ \mu\text{m}$ photometry, so their temperatures may be systematically higher and dust masses lower compared with our analysis, although this should not lead them to over-estimate m_{32} unless the bias is greater at low L_{CO} . Corbelli et al. (2012) fitted correlations between $L_{(3-2)}$ and luminosities in each of the PACS and SPIRE bands, finding roughly linear slopes and an evolution in the slope from short to long wavelengths. We see some tentative evidence for a similar wavelength dependence of the slope in the right-hand panel of Figure 4, and this is qualitatively consistent with the difference between n_{32} (\sim slope of the short-wavelength luminosity correlation) and m_{32} (\sim slope of the long-wavelength luminosity correlation).

The negative slope of $M_{\text{dust}}/L_{\text{CO}}$ versus L_{CO} in Figure 8 indicates an intrinsic variation across the sample. This variation could be in the dust/ H_2 ratio, the CO/ H_2 ratio, or the CO excitation. To explore the possible dependence on metallicity, we can plot the ratios against stellar mass, which is correlated with metallicity. As a result, more massive galaxies are expected to have higher dust/gas ratios, but they also have lower gas/stellar mass fractions, both from CO(1–0) (Saintonge et al., 2011) and HI (Cortese et al. 2011; Catinella et al., 2012), and lower dust/stellar mass fractions (Bourne et al., 2012; Cortese et al., 2012). Figure 10 shows that the dust/HI mass fraction increases and the HI/stellar mass fraction decreases with stellar mass, as we expect (and as shown by Cortese et al. 2012). In Figure 11, however, $M_{\text{dust}}/L_{(3-2)}$ appears to weakly decrease with increasing M_* , while $M_{\text{dust}}/L_{(2-1)}$ is not significantly correlated with M_* , which does not follow the expected behaviour of the dust/ H_2 ratio. Similarly, neither $L_{(3-2)}/M_*$ nor $L_{(2-1)}/M_*$ show any anticorrelation with stellar mass, which we would expect in the M_{H_2}/M_* ratio. These correlations may therefore be confounded by metallicity variations, which could reduce both the dust/ H_2 and CO/ H_2 ratios at low stellar masses. Note for example the low CO content of low-metallicity dwarfs in comparison with expectations from the SK law (Schrubba et al., 2012) and in comparison with the [CII] molecular gas tracer (Smith & Madden 1997; Hunter et al., 2001; Israel & Maloney 2011; Madden et al., 2012).

We might expect less scatter in Figure 11 using CO(1–0), which is a closer tracer of the total CO mass (and M_{H_2} , given X_{CO}), in which case the large scatter we see in the CO(3–2) and CO(2–1) ratios is a result of different excitation conditions across the sample. However, this explanation is difficult to reconcile with the fact that greater scatter is observed in the CO(2–1) than CO(3–2) correlations. To test whether a correlation between L_{CO} and excitation could explain the decreasing $M_{\text{dust}}/L_{\text{CO}}$ in Figure 8, we measure a slope of -0.48 ± 0.05 in $\log(M_{\text{dust}}/L_{(3-2)})$ as a function of $\log(L_{(3-2)})$. If $M_{\text{dust}}/L_{(1-0)}$ is constant, then the

R_{31} line ratio must vary by a factor of 10 ± 1 over the range $7.2 < \log(L_{(3-2)}) < 9.5$ in order to explain the observed trend. In conclusion, to translate the trends in $M_{\text{dust}}/L_{(2-1)}$ into $M_{\text{dust}}/M_{\text{H}_2}$ (and hence total gas-to-dust), we need either global CO(1–0) or gas-phase metallicity measurements.

5 CONCLUSIONS

We have measured the global fluxes in the CO(2–1) and CO(3–2) lines in a pilot sample of nearby galaxies selected in the submm from H-ATLAS. We exploit the wide areal coverage of H-ATLAS to blindly select at $500\ \mu\text{m}$, thus sampling low-redshift galaxies with the highest dust masses, a population that is relatively poorly studied in the local Universe. Galaxies in the sample are a mixture of dust-rich late-type spirals, starbursts, merging/interacting galaxies, low-surface-brightness disks, and dusty early-type galaxies. We analyse the results in terms of the correlations between different tracers of dust and gas in the ISM, using 22– $500\ \mu\text{m}$ photometry from H-ATLAS, *IRAS*, and *WISE*, and HI 21 cm line fluxes from HIPASS and from the literature. Our conclusions are as follows:

(i) We measure correlations between the CO and IR fluxes in all FIR and submm bands from 22 to $500\ \mu\text{m}$, and find that scatter in the correlations evolves with the IR wavelength used. The CO(3–2) line is better correlated with FIR bands close to the $\sim 100\ \mu\text{m}$ peak of the SED, consistent with it being a dense gas tracer and the FIR being correlated with SFR. The CO(2–1) line appears to be better correlated with the submm rather than FIR bands near the peak, although this needs to be confirmed with a larger sample. It is clear that the CO(2–1)–IR correlations have a different wavelength dependence to the CO(3–2)–IR correlations, consistent with CO(2–1) and CO(3–2) tracing different components of the molecular gas.

(ii) In correlations between the HI 21 cm line and the FIR/submm, the scatter follows opposite trends with wavelength to the CO(3–2). This indicates that the submm, which traces the cold dust mass, is also better correlated with the neutral atomic gas (which is robustly traced by the HI line) than the shorter FIR wavelengths. These results suggest that the FIR luminosity ($\sim 100\ \mu\text{m}$) traces the SFR due to the correlation with dense gas, while the submm is more closely correlated with the total gas mass due to the better correlation with HI [and CO(2–1)]. We caution, however, that in these submm-selected galaxies, even the $100\ \mu\text{m}$ fluxes contain significant emission from cold cirrus dust.

(iii) Differential correlation strengths as a function of wavelength are interpreted as evidence for dust at different temperatures occupying different phases of the ISM, with warm dust being more associated with dense molecular gas clouds, and cold dust inhabiting the diffuse neutral (HI) ISM. This is consistent with cold dust being at least partially heated by radiation from older stellar populations rather than young OB stars, as shown by independent evidence (e.g. Boquien et al. 2011; Bendo et al. 2012; Boselli et al. 2012).

(iv) We observe a deviation from the trends described above when considering 22 and $60\ \mu\text{m}$ fluxes. These show a poorer correlation with CO(3–2) than fluxes at longer wavelengths, while $22\ \mu\text{m}$ fluxes are better correlated with HI

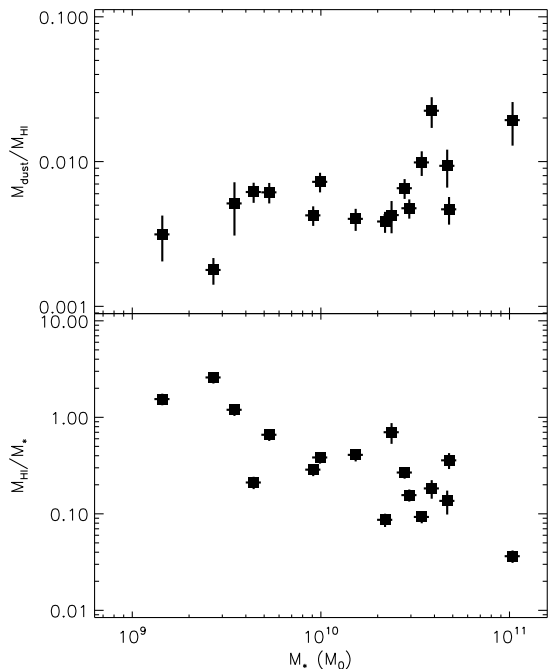


Figure 10. Dust-to-HI mass ratio and HI-to-stellar mass ratio as a function of stellar mass.

than fluxes at longer wavelengths. This can be explained by a contribution to this part of the IR SED by stochastically-heated very small grains in the diffuse phase of the ISM.

(v) The slope (n) of the FIR–CO correlation appears to be sub-linear in this sample: we fit $L_{\text{FIR}} \propto L_{\text{CO}}^n$ with $n = 0.77 \pm 0.10$ for CO(3–2) and $n = 0.80 \pm 0.27$ for CO(2–1). These values are lower than that measured in most other samples (Yao et al. 2003; Iono et al. 2009; Mao et al. 2010), although the relatively small number of data points and small luminosity range in this sample may account for the difference.

(vi) We also find significantly sub-linear slopes of $m_{32} = 0.60 \pm 0.08$ and $m_{21} = 0.47 \pm 0.20$ in the $M_{\text{dust}} \propto L_{(3-2)}^{m_{32}}$ and $M_{\text{dust}} \propto L_{(3-2)}^{m_{21}}$ correlations respectively, in comparison to approximately linear slopes in the $60 \mu\text{m}$ SLUGS sample (Yao et al. 2003) and the Virgo cluster spirals in HeVICS (Corbelli et al. 2012). The explanation for these slopes could be a large range of metallicity across this sample, with higher-mass galaxies having higher metallicity, hence higher CO/ H_2 and lower dust/CO ratios for the same dust/gas ratio. CO excitation may also play a role, since this is likely to correlate with luminosity, but a variation in R_{31} by a factor of 10 ± 1 between $7.2 < \log(L_{(3-2)}) < 9.5$ would be required to fully explain the trend if the underlying $M_{\text{dust}}/M_{\text{CO}}$ ratio is constant.

(vii) The FIR/CO luminosity ratios of this sample are in line with low/moderate luminosity SFGs in the local Universe, and not with (U)LIRGs and high-redshift SMGs, suggesting that the dustiest galaxies at low redshifts have modest star-formation efficiencies (= SFR/gas mass).

This pilot study of a small sample has revealed some

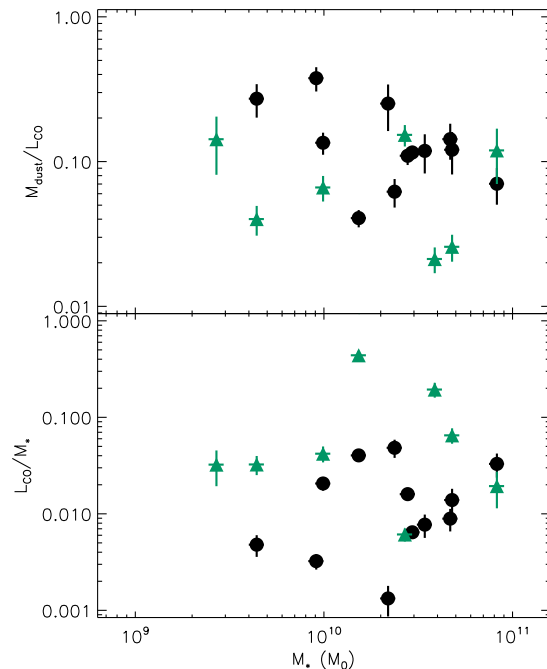


Figure 11. Dust-to- L_{CO} ratio and L_{CO} -to-stellar mass ratio as a function of stellar mass.

interesting trends in the correlation of various gas tracers with the FIR and submm, but many questions remain unanswered. Additional data for CO(2–1) and CO(1–0) in particular would enable a better understanding of the correlations between total CO mass and the FIR/submm, and by comparing to H_2 gas masses estimated from the dust mass, it would be possible to investigate any variation of the CO X factor in these dust- and gas-rich (and potentially high-metallicity) galaxies. Observations of [C I] emission with ALMA (currently available at intermediate redshifts in band 7) would also be valuable for such a comparison, and would improve our ability to interpret measurements of the more commonly observed CO lines.

ACKNOWLEDGEMENTS

The authors thank the referee for his/her helpful insights on the paper. The *Herschel*-ATLAS is a project with *Herschel*, which is an ESA space observatory with science instruments provided by European-led Principal Investigator consortia and with important participation from NASA. The H-ATLAS website is <http://www.h-atlas.org/>. The James Clerk Maxwell Telescope is operated by the Joint Astronomy Centre on behalf of the Science and Technology Facilities Council of the United Kingdom, the Netherlands Organisation for Scientific Research, and the National Research Council of Canada. This paper makes use of data obtained from the JCMT proposal M11AU04. The Parkes telescope is part of the Australia Telescope which is funded by the Commonwealth of Australia for operation as a National Facility managed by CSIRO. This publication makes use of

data products from the Wide-field Infrared Survey Explorer, which is a joint project of the University of California, Los Angeles, and the Jet Propulsion Laboratory/California Institute of Technology, funded by the National Aeronautics and Space Administration. This research has made use of the NASA/IPAC Extragalactic Database (NED), and the NASA/IPAC Infrared Science Archive, which are operated by the Jet Propulsion Laboratory, California Institute of Technology, under contract with the National Aeronautics and Space Administration.

References

- Abazajian K. N., et al., 2009, *ApJS*, 182, 543
 Albrecht M., Krügel E., Chini R., 2007, *A&A*, 462, 575
 Barnes D. G., et al., 2001, *MNRAS*, 322, 486
 Bell E. F., 2003, *ApJ*, 586, 794
 Bendo G. J., et al., 2010a, *A&A*, 518, L65
 Bendo G. J., et al., 2010b, *MNRAS*, 402, 1409
 Bendo G. J., et al., 2012, *MNRAS*, 419, 1833
 Böker T., Lisenfeld U., Schinnerer E., 2003, *A&A*, 406, 87
 Boquien M., et al., 2011, *AJ*, 142, 111
 Boselli A., et al., 2010, *A&A*, 518, L61
 Boselli A., et al., 2012, *A&A*, 540, A54
 Bothwell M. S., et al., 2013, *MNRAS*, 429, 3047
 Boulanger F., Perault M., 1988, *ApJ*, 330, 964
 Bourne N., et al., 2012, *MNRAS*, 421, 3027
 Braine J., Combes F., Casoli F., Dupraz C., Gerin M., Klein U., Wielebinski R., Brouillet N., 1993, *A&AS*, 97, 887
 Braun R., 2012, *ApJ*, 749, 87
 Calzetti D., et al., 2010, *ApJ*, 714, 1256
 Catinella B., et al., 2012, *A&A*, 544, A65
 Chabrier G., 2003, *PASP*, 115, 763
 Clemens M. S., et al., 2013, *MNRAS*, 433, 695
 Coccato L., Morelli L., Corsini E. M., Buson L., Pizzella A., Vergani D., Bertola F., 2011, *MNRAS*, 412, L113
 Compiègne M., et al., 2011, *A&A*, 525, A103
 Condon J. J., 1992, *ARA&A*, 30, 575
 Condon J. J., Cotton W. D., Greisen E. W., Yin Q. F., Perley R. A., Taylor G. B., Broderick J. J., 1998, *AJ*, 115, 1693
 Corbelli E., et al., 2012, *A&A*, 542, A32
 Cortese L., Catinella B., Boissier S., Boselli A., Heinis S., 2011, *MNRAS*, 415, 1797
 Cortese L., et al., 2012, *A&A*, 540, A52
 Cox P., Kruegel E., Mezger P. G., 1986, *A&A*, 155, 380
 da Cunha E., Charlot S., Elbaz D., 2008, *MNRAS*, 388, 1595
 Daddi E., et al., 2010, *ApJL*, 714, L118
 Dale D. A., Helou G., 2002, *ApJ*, 576, 159
 Davies J. I., et al., 2010, *A&A*, 518, L48
 Davies J. I., et al., 2012, *MNRAS*, 419, 3505
 de Jong T., Clegg P. E., Rowan-Robinson M., Soifer B. T., Habing H. J., Houck J. R., Aumann H. H., Raimond E., 1984, *ApJ*, 278, L67
 de Vaucouleurs G., de Vaucouleurs A., Corwin H. G., Buta R. J., Paturel G., Fouqué P., 1991, *Third Reference Catalogue of Bright Galaxies. Volume I: Explanations and references. Volume II: Data for galaxies between 0h and 12h. Volume III: Data for galaxies between 12h and 24h.* Springer, New York, NY
 Devereux N. A., Young J. S., 1990, *ApJ*, 359, 42
 Dickman R. L., Snell R. L., Schloerb F. P., 1986, *ApJ*, 309, 326
 Draine B. T., Anderson N., 1985, *ApJ*, 292, 494
 Draine B. T., et al., 2007, *ApJ*, 663, 866
 Driver S. P., et al., 2011, *MNRAS*, 413, 971
 Dunne L., Eales S., Edmunds M., Ivison R., Alexander P., Clements D. L., 2000, *MNRAS*, 315, 115
 Dunne L., Eales S. A., 2001, *MNRAS*, 327, 697
 Eales S., et al., 2010, *PASP*, 122, 499
 Engel H., et al., 2010, *ApJ*, 724, 233
 Feldmann R., Gnedin N. Y., Kravtsov A. V., 2012, *ApJ*, 758, 127
 Galametz M., Madden S. C., Galliano F., Hony S., Bendo G. J., Sauvage M., 2011, *A&A*, 532, A56
 Gallimore J. F., et al., 2010, *ApJS*, 187, 172
 Gao Y., Solomon P. M., 2004, *ApJ*, 606, 271
 Genzel R., et al., 2010, *MNRAS*, 407, 2091
 Genzel R., et al., 2012, *ApJ*, 746, 69
 Greve T. R., et al., 2005, *MNRAS*, 359, 1165
 Griffin M. J., et al., 2010, *A&A*, 518, L3
 Groves B., et al., 2012, *MNRAS*, 426, 892
 Hatziminaoglou E., et al., 2010, *A&A*, 518, L33
 Haynes M. P., Giovanelli R., 1984, *AJ*, 89, 758
 Heidmann J., Heidmann N., de Vaucouleurs G., 1972, *Memoirs of the Royal Astronomical Society*, 75, 85
 Helfer T. T., Thornley M. D., Regan M. W., Wong T., Sheth K., Vogel S. N., Blitz L., Bock D. C.-J., 2003, *ApJS*, 145, 259
 Helou G., 1986, *ApJ*, 311, L33
 Hill D. T., et al., 2011, *MNRAS*, 412, 765
 Hunt L., et al., 2012, *MNRAS*, 427, 906
 Hunter D. A., et al., 2001, *ApJ*, 553, 121
 Ibar E., et al., 2010, *MNRAS*, 409, 38
 Iono D., et al., 2009, *ApJ*, 695, 1537
 Ishihara D., et al., 2010, *A&A*, 514, 1
 Israel F. P., et al., 1984, *A&A*, 134, 396
 Israel F. P., Maloney P. R., 2011, *A&A*, 531, A19
 Issa M. R., MacLaren I., Wolfendale A. W., 1990, *A&A*, 236, 237
 Ivison R. J., Papadopoulos P. P., Smail I., Greve T. R., Thomson A. P., Xilouris E. M., Chapman S. C., 2011, *MNRAS*, 412, 1913
 James A., Dunne L., Eales S., Edmunds M. G., 2002, *MNRAS*, 335, 753
 Kennicutt R. C., 1998a, *ApJ*, 498, 541
 Kennicutt R. C., 1998b, *ARA&A*, 36, 189
 Kennicutt R. C., Evans N. J., 2012, *ARA&A*, 50, 531
 Komugi S., et al., 2011, *PASJ*, 63, 1139
 Koribalski B. S., et al., 2004, *AJ*, 128, 16
 Krumholz M. R., Dekel A., McKee C. F., 2012, *ApJ*, 745, 69
 Krumholz M. R., Thompson T. A., 2007, *ApJ*, 669, 289
 Lang R. H., et al., 2003, *MNRAS*, 342, 738
 Lara-López M. A., López-Sánchez Á. R., Hopkins A. M., 2013, *ApJ*, 764, 178
 Leroy A. K., et al., 2011, *ApJ*, 737, 12
 Leroy A. K., et al., 2013, *AJ*, 146, 19
 Li A., Draine B. T., 2001, *ApJ*, 554, 778
 Lisenfeld U., Ferrara A., 1998, *ApJ*, 496, 145

- Madden S. C., et al., 2012, in Tuffs R. J., Popescu C. C., eds, IAU Symposium Vol. 284, Low Metallicity ISM: excess submillimetre emission and CO-free H₂ gas. pp 141–148
- Magdis G. E., et al., 2011, ApJ, 740, L15
- Magrini L., et al., 2011, A&A, 535, A13
- Malhotra S., et al., 2001, ApJ, 561, 766
- Mannucci F., Cresci G., Maiolino R., Marconi A., Gnerucci A., 2010, MNRAS, 408, 2115
- Mao R.-Q., Schulz A., Henkel C., Mauersberger R., Muders D., Dinh-V-Trung 2010, ApJ, 724, 1336
- Meyer M. J., et al., 2004, MNRAS, 350, 1195
- Moshir M., Kopman G., Conrow T. A. O., 1992, IRAS Faint Source Survey, Explanatory supplement version 2. Infrared Processing and Analysis Center, California Institute of Technology, Pasadena, CA
- Muñoz-Mateos J. C., et al., 2009, ApJ, 701, 1965
- Murakami H., et al., 2007, PASJ, 59, 369
- Murphy E. J., et al., 2012, ApJ, 761, 97
- Narayanan D., Cox T. J., Shirley Y., Davé R., Hernquist L., Walker C. K., 2008, ApJ, 684, 996
- Narayanan D., Krumholz M. R., Ostriker E. C., Hernquist L., 2012, MNRAS, 421, 3127
- Negrello M., et al., 2010, Science, 330, 800
- Neugebauer G., et al., 1984, ApJ, 278, L1
- Pascale E., et al., 2011, MNRAS, 415, 911
- Paturel G., Petit C., Prugniel P., Theureau G., Rousseau J., Brouty M., Dubois P., Cambrésy L., 2003, A&A, 412, 45
- Pierini D., Lequeux J., Boselli A., Leech K. J., Völk H. J., 2001, A&A, 373, 827
- Pilbratt G. L., et al., 2010, A&A, 518, L1
- Poglitsch A., et al., 2010, A&A, 518, L2
- Press W. H., Teukolsky S. A., Vetterling W. T., Flannery B. P., 2007, Numerical Recipes 3rd Edition: The Art of Scientific Computing. Cambridge University Press
- Rigby E. E., et al., 2011, MNRAS, 415, 2336
- Rohlfs K., Wilson T. L., 2006, Tools of Radio Astronomy. Springer, Heidelberg, Germany
- Rowan-Robinson M., et al., 2010, MNRAS, 409, 2
- Rowlands K., et al., 2012, MNRAS, 419, 2545
- Saintonge A., et al., 2011, MNRAS, 415, 61
- Sakamoto S., Hasegawa T., Hayashi M., Handa T., Oka T., 1995, ApJS, 100, 125
- Sanders D. B., Mazzarella J. M., Kim D.-C., Surace J. A., Soifer B. T., 2003, AJ, 126, 1607
- Sauty S., et al., 2003, A&A, 411, 381
- Schmidt M., 1959, ApJ, 129, 243
- Schruba A., et al., 2012, AJ, 143, 138
- Schweitzer M., et al., 2006, ApJ, 649, 79
- Skrutskie M. F., et al., 2006, AJ, 131, 1163
- Smith B. J., Madden S. C., 1997, AJ, 114, 138
- Smith D. J. B., et al., 2011, MNRAS, 416, 857
- Smith D. J. B., et al., 2012a, MNRAS, 427, 703
- Smith M. W. L., et al., 2012b, ApJ, 756, 40
- Smith M. W. L., et al., 2012c, ApJ, 748, 123
- Soifer B. T., Boehmer L., Neugebauer G., Sanders D. B., 1989, AJ, 98, 766
- Taylor E. N., et al., 2011, MNRAS, 418, 1587
- Totani T., Takeuchi T. T., Nagashima M., Kobayashi M. A. R., Makiya R., 2011, PASJ, 63, 1181
- Tremaine S., et al., 2002, ApJ, 574, 740
- Tremonti C. A., et al., 2004, ApJ, 613, 898
- Vergani D., Pizzella A., Corsini E. M., van Driel W., Buson L. M., Dettmar R.-J., Bertola F., 2007, A&A, 463, 883
- Vila-Costas M. B., Edmunds M. G., 1992, MNRAS, 259, 121
- Vlahakis C., Dunne L., Eales S., 2005, MNRAS, 364, 1253
- Walter F., et al., 2007, ApJ, 661, 102
- Walterbos R. A. M., Greenawalt B., 1996, ApJ, 460, 696
- Walterbos R. A. M., Schwering P. B. W., 1987, A&A, 180, 27
- Wilson C. D., et al., 2009, ApJ, 693, 1736
- Wilson C. D., et al., 2012, MNRAS, p. 3401
- Wong O. I., et al., 2006, MNRAS, 371, 1855
- Wright E. L., et al., 2010, AJ, 140, 1868
- Xu C., Helou G., 1994, ApJ, 426, 109
- Yamamura I., et al., 2009, in Usuda T., Tamura M., Ishii M., eds, American Institute of Physics Conference Series Vol. 1158. pp 169–170
- Yao L., Seaquist E. R., Kuno N., Dunne L., 2003, ApJ, 588, 771
- Young J. S., et al., 1995, ApJS, 98, 219
- Zwaan M. A., Briggs F. H., Sprayberry D., Sorar E., 1997, ApJ, 490, 173